POLITECNICO DI TORINO

Master of Science in Mechanical Engineering

Master thesis

Diluted combustion CFD analysis in a SI engine running on hydrogen-NG blends

Supervisor:

Prof. Daniela Anna MISUL

Prof. Mirko BARATTA

Candidate:

Antonio DE CANDIA

Luglio 2019

Abstract

In the modern scenario of pollutant emission regulation, the next EU fleet-wide average emission target to be reached before 2021 for new cars, is 95 g CO_2/km. Because of high hydrogen to carbon ratio, methane is capable to reduce significantly CO_2 emissions, with respect to a gasoline or diesel engine of the same power output. Moreover, methane is potential fuel for large scale supply and it is characterized by high octane rating which can help in increasing engine efficiency by operating with higher compression ratios.

The present work has been carried out in a research team in DENERG laboratory at Politecnico di Torino. The aim of the thesis is the development of a model for 3D CFD simulations of an internal combustion engine fueled with natural gas, using CONVERGE CFD software. Once the model has been calibrated and validated with experimental data, for pure methane and two different mixture of hydrogen and natural gas (HCNG blends), it is used to predict the behaviour of the engine in case of dilution with exhaust gas (EGR) in different percentage. The post-processing analysis is focused on the combustion process and in particular on the effect of hydrogen addition, exhaust gas recirculation (EGR) and turbulence intensity on the stability of combustion and on the flame propagation in the chamber. One of the drawbacks in the use of natural gas is the slow burning velocity. This parameter can be however increased by adding hydrogen, thus reducing the combustion duration and improving the flame development. Another powerful way to increase the burning speed is the increase of turbulence inside the chamber: this causes higher wrinkling of the flame and faster exchange of heat and mixing of species. In this way the overall combustion process results to be substantially improved.

Summary

List of Figures

List of Tables

Introduction

Natural gas (NG) represents an effective alternative to traditional fuels thanks to reduced carbon dioxide emissions and potential for large scale supply. In fact, methane that is the primary constituent of NG has the highest molecular hydrogen-to-carbon ratio of all hydrocarbons, which allows a potential of 20% CO_2 reduction as compared to the long-chained molecules found in Diesel oil and gasoline. NG has a narrow range of flammability and a high auto-ignition temperature of 813 K (540 °C). Generally, it can be stored in vehicles with the form of compressed natural gas (CNG) under 20 MPa or liquefied natural gas (LNG) under very low temperature (– 162 °C) at atmospheric pressure. There are three basic application modes for NG engines or vehicles: pure NG engines/vehicles including CNG and LNG, gasoline/NG bi-fuel mode refitted from spark ignition (SI) gasoline engines, and diesel/NG dual fuel (DF) mode based on compression ignition (CI) diesel engines. The most distinctive feature is that NG vehicles are commonly applied in the transport sector, as it is shown in Figure 1. NG/gasoline bi-fuel vehicles are used on taxies, and a little on modified private cars, which are strictly restrained. CNG vehicles are applied on taxies, city buses and trucks. To keep the running mileage, LNG engines are equipped on intercity buses or long-way passenger vehicles and they are also applied on trucks because they have higher energy density. Moreover, a few heavy-duty vehicles use NG/diesel dual-fuel engines [1].

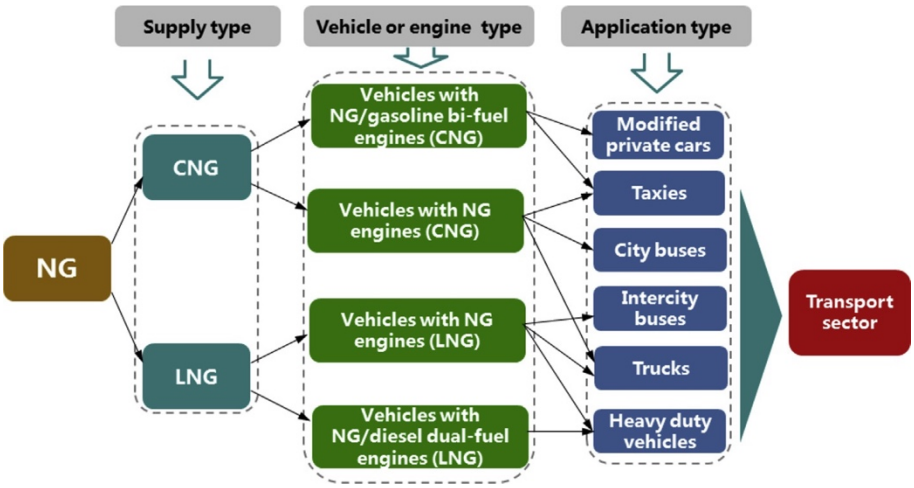

Figure 1: Classification of NG engine type and application

In the SI engine, direct injection (DI) technology can significantly increase the engine volumetric efficiency and reduce "pumping losses" in engines without a throttle valve. DI

allows engine operation with the stratified charge which enables relatively higher combustion efficiency [2]. CNG-DI avoids the fresh air displacement by direct fuel injection into the cylinder after intake valve closing, thus increasing the volumetric efficiency.

The use of EGR with advanced turbocharging and diluted combustion is another important trend. With specific reference to diluted combustion, it is rather well established for gasoline engines whereas it still poses several critical issues for CNG ones, mainly due to the lower exhaust temperatures. Moreover, dilution is accompanied by a decrease in the laminar burning speed of the unburned mixture and this generally leads to a detriment in combustion efficiency and stability. The optimization of in-cylinder turbulence plays a fundamental role in compensating these effects [3].

Key-feature of NG is its high octane number which can help in increasing engine efficiency by operating with higher compression ratios. This indicates high knock resistance as a promising enabling factor for extracting more power from a given engine displacement and therefore increasing engine specific power. NG engines operating with high compression ratio and boost pressure level as well as lean-burn approach or heavy exhaust gas recirculation could be equivalent to their gasoline counterparts in terms of available torque and power, allowing also a substantial reduction in pollutant emissions and improvement in engine thermal efficiency. However, when fueled with NG, the bi-fuel vehicles cannot improve the thermal efficiency by increasing the compression ratio (CR), to meet the requirement of antiknock for gasoline. In other words, the advantages of NG cannot be exhibited in bi-fuel mode.

CNG features lower burning speed and reduced volumetric efficiency with respect to conventional liquid fuels. Such drawbacks and the corresponding penalties on the engine behavior can be overcome to some extent by the advantages connected to the use of hydrogen as an additive. Hydrogen would represent a practical alternative to gasoline thanks to its higher mass specific lower heating value (LHV), nearly three times the one of methane or gasoline, and to the higher efficiencies and reduced emissions. The problem is represented by the lack of distribution infrastructure that limits its use to a mere additive or to dual fuel operations [4]. Generally, hydrogen addition reduces combustion duration, increases break thermal efficiency, extends lean burn range, and reduces carbon dioxide amounts [5]. The simulation of laminar flame speed manifests that the addition of H_2 increases the concentration of H and OH radicals and hence improves the flame propagation and the combustion process, resulting in an improved laminar flame speed of the fuel-air mixtures. CO_2 emission reduction at engine exhaust is strictly related to the amount of NG substitution with H_2 content. Furthermore, HC

and CO emissions of HCNG engines are decreased with H_2 addition, and NOx is increased due to the combustion temperature elevation.

In the present work the performances of a turbocharged 1.4 liter engine, originally designed to run on CNG, are studied with the use of CFD simulations. Computational fluid dynamics (CFD) allows to numerically solve the equations of fluid motion to produce quantitative predictions and/or analyses of fluid flow phenomena. Indeed, CFD is often ideal for parametric investigations or flow-physics that would otherwise be impractical or impossible via entirely theoretical or experimental efforts. In particular, in internal combustion engine field CFD can be a powerful and efficient way to deeply understand the phenomena that take place inside the engine, capturing the characteristics of the fluid during the working cycle, and give a realistic idea of the best results and/or compromises that could be obtained on the actual machine. For this purpose, a 3D numerical model for the in-cylinder turbulence and combustion simulation has been developed in CONVERGE CFD software. The model embeds a user-specified laminar flame speed sub-model, which was derived from a 1-D combustion simulation model with detailed chemistry. The effect of hydrogen addition and EGR dilution are investigated and the analysis is focused on their influence on combustion duration, in particular in the early stage of the process.

In the final part, the burning velocity developed in the engine studied are computed, based on a spherically expanding flame model, and compared with those of a high-turbulence engine, in order to assess the effect of turbulence on flame propagation in the chamber. For what stated before regarding the improvement in terms of CO_2 emissions given by the usage of engines running on hydrogen-NG blends, the characterization proposed by the present work results to be desirable in a near future perspective where this kind of alternative fuels will be, for sure, one of the primary choices in the propulsion scenario.

1. Computational Fluid Dynamics

1.1 CFD for ICE Applications

Computational fluid dynamics (CFD) is the rapidly evolving science of numerically solving the equations of fluid motion to produce quantitative predictions and/or analyses of fluid flow phenomena. These predictions normally occur under those conditions defined in terms of the flow geometry, the physical properties of a fluid, and the boundary and initial conditions of a flow field. Such predictions generally concern sets of values of the flow variables: velocity, pressure, or temperature at selected locations in the domain and for selected times. The predictions may also involve evaluations of overall flow behaviour, such as the flow rate or the hydrodynamic force acting on an object in the flow. When used appropriately, CFD is often ideal for parametric studies or flow-physics investigations that would otherwise be impractical or impossible via entirely theoretical or experimental efforts [6].

As a research and design tool, CFD normally complements experimental and theoretical fluid dynamics. In this regard, CFD has a number of distinct advantages:

- It can be produced inexpensively and quickly, without an extraordinary amount of training, although interpreting results often requires experience.
- It generates complete information. Full-field CFD produces detailed and comprehensive information of all relevant variables throughout the domain of interest. This information can also be easily accessed.
- It allows for easy parameter changes. CFD permits input parameters to be varied easily over wide ranges, thereby facilitating design optimization. Such variations are often either impossible or prohibitively expensive in experimental studies.
- It has the ability to simulate realistic conditions. CFD can simulate flows directly under practical conditions, unlike experiments, where a small- or a large-scale model may be needed, or analytical theories that may only be valid for limiting cases where one parameter or another is very large or small.
- It has the ability to simulate ideal conditions. CFD provides the convenience of switching off certain terms in the governing equations, which allows one to focus the attention on a

few essential parameters and eliminate all irrelevant features. Such parametric control is typically impossible in experiments.

- It permits investigation of unnatural or unwanted situations. CFD allows events to be studied so that every attempt is made to prevent, for example, conflagrations, explosions, or nuclear power plant failures.

The dominant approaches to CFD are the finite-difference and finite-volume or finite-element formulations. In both cases, CFD involves discretizing the spatial domain into a grid or mesh of points or elements and marching the numerical solution forward in discrete time steps.
In recent years, this important tool has been used in industrial environment to improve the design process of machines and components that deals with fluid interaction. In particular, in internal combustion engine field CFD can be a powerful and efficient way to analyse the behaviour of the engine in the different phases of the working cycle and different operating points, capturing the characteristics of the fluid, and deeply understanding the phenomena that take place inside the engine. 3D CFD simulations can give sufficiently accurate results on performances of the engine and a realistic idea of the best results and/or compromises that could be obtained on the actual machine. This allows doing tests that were not performed experimentally, with a decrease in costs for the development of the engine itself. Once the model has been set up and verified with experimental results, different simulations can be performed, and results are available in relatively short period of time.
Modern 3D CFD software give a wide opportunity of parameters that can be changed in order to see the effects on the engine, such as spark advance, lift profiles of the valves, spray profiles for the injectors, boundary conditions, Exhaust Gas Recirculation (EGR) and fuel composition; each one of these parameters has to be set accordingly with the type of simulation that has to be run. Moreover, even the use of multiple fuels inside the chamber can be simulated and analysed.

1.2 Navier-Stokes system of equations

In the present section, a brief review of the governing principles in fluid mechanics is given. The conservation laws for mass, momentum, and energy are presented. In particular, the laws

can be stated in integral form, applicable to an extended region, or in differential form, applicable at a point or to a fluid particle.

1.2.1 Mass conservation

The mass conservation, also known as *continuity equation*, is based on the principle that the mass of a specific collection of neighbouring fluid particles is constant. The continuity equation relies on the concept of control volume V(t)that is the volume occupied by a specific collection of fluid particles. In particular, such a volume moves and deforms within a fluid flow so that it always contains the same mass elements. The law can be written in integral form (1), where the first member represents the variation in time of the mass while the second term takes into account the mass transport into the control volume.

$$\int_V \frac{\partial \rho}{\partial t} dV + \int_S \rho \boldsymbol{u} \cdot \boldsymbol{n}\, dS = 0 \tag{1}$$

Where:

ρ is the density of the fluid;

$\boldsymbol{u}$ is the velocity vector;

S is the surface or boundary of the control volume V;

$\boldsymbol{n}$ is the normal versor to the surface.

Applying Gauss theorem, the mass conservation can be written in differential form:

$$\frac{\partial \rho}{\partial t} + \nabla \cdot (\rho \boldsymbol{u}) = 0 \tag{2}$$

1.2.2 Momentum conservation

The momentum is defined as the product between the velocity and the density, so it is a vectorial quantity. Its conservation comes directly from Newton's second law:

$$\int_V \frac{\partial \rho \boldsymbol{u}}{\partial t} dV + \int_S \rho \boldsymbol{u}\boldsymbol{u} \cdot \boldsymbol{n}\, dS = \sum_i f \tag{3}$$

The momentum law is composed by a first term, which represents the rate of change of momentum in time, a second term which is the transport term, while the term on the right-hand side (RHS) represents the sum of all external forces acting in the control volume. The external forces can be body forces (like gravitational force, Coriolis force, electromagnetic force, etc.) or surface forces (pressure, surface tension, normal and shear stresses, etc.). In order to have the closure of the system of equations, some assumptions are needed, so that the terms corresponding to the fluxes of surface forces are expressed as function of the system variables and the flow can be resolved.

The most common assumption is that the fluid is a Newtonian fluid so that the stress tensor can be expressed as a function of the velocity:

$$\boldsymbol{\sigma} = -pI + \mu\left[\nabla\boldsymbol{u} + (\nabla\boldsymbol{u})^T - \frac{2}{3}(\nabla\cdot\boldsymbol{u})I\right] \tag{4}$$

Where:

p is the static pressure;

μ is the dynamic viscosity of the fluid.

Introducing the term (4) into equation (3), the conservation of momentum in integral form becomes:

$$\int_V \frac{\partial\rho\boldsymbol{u}}{\partial t}\,dV + \int_S \rho\boldsymbol{u}\boldsymbol{u}\cdot\boldsymbol{n}\,dS = \int_S \boldsymbol{\sigma}\cdot\boldsymbol{n}\,dS + \int_V \rho\boldsymbol{b}\,dV \tag{5}$$

Where $\boldsymbol{b}$ takes into account the body forces. Applying Gauss theorem, it is possible to express the differential form of the momentum equation:

$$\frac{\partial\rho\boldsymbol{u}}{\partial t} + \nabla\cdot(\rho\boldsymbol{u}\boldsymbol{u}) = \nabla\cdot\boldsymbol{\sigma} + \rho\boldsymbol{b} \tag{6}$$

1.2.3 Energy conservation

The energy equation is the mathematical expression of the first law of thermodynamics, also called the *principle of conservation of energy*, which states that heat is actually a form of energy; Heat energy, therefore, cannot be created or destroyed; nevertheless, it can be

transferred from one location to another and converted to and from other forms of energy. The conserved quantity is the total energy, defined as the sum of internal energy and kinetic energy. The rate of change of energy is equal to the sum of the rate of heat added to the system and the rate of work done on a fluid particle by the surface forces and body forces. The integral formulation of the energy equation is:

$$\int_V \frac{\partial e_{tot}}{\partial t} dV + \int_S \rho e_{tot} \boldsymbol{u} \cdot \boldsymbol{n}\, dS = \int_S \boldsymbol{q} \cdot \boldsymbol{n}\, dS + \int_S (\boldsymbol{\sigma} \cdot \boldsymbol{u}) \cdot \boldsymbol{n}\, dS + \int_V \rho \boldsymbol{b} \cdot \boldsymbol{u}\, dV \tag{7}$$

Where:

$e_{tot} = e_i + \frac{1}{2}\boldsymbol{u} \cdot \boldsymbol{u}$ is the total energy per unit mass;

$\boldsymbol{q} = -k\nabla T$ is the conductive heat flux (Fourier's Law) and k is the thermal conductivity.

The differential form of the energy conservation law, obtained applying the Gauss theorem, is the following:

$$\frac{\partial e_{tot}}{\partial t} + \nabla \cdot (\rho e_{tot} \boldsymbol{u}) = \nabla \cdot \boldsymbol{q} + \nabla \cdot (\boldsymbol{\sigma} \cdot \boldsymbol{u}) + \rho \boldsymbol{b} \cdot \boldsymbol{u} \tag{8}$$

The energy equation can be turned into another formulation, called the *Heat equation*, by neglecting the viscous heating and the compressibility effect:

$$\rho c_p \frac{\partial T}{\partial t} + \rho c_p \boldsymbol{u} \cdot \nabla T = \nabla \cdot (k \nabla T) \tag{9}$$

1.3 Discretization methods

Fluid flows and related phenomena can be described by partial differential equations that cannot be solved analytically except in special cases. To obtain an approximate solution numerically, discretization methods are needed; in this way, the differential equations are approximated by

a system of algebraic equations for the variables at some set of discrete locations in space and time [7]. Besides the most famous discretization methods there are:

- Finite Differences method (FD): it is the easier method to use for simple geometries. The solution domain is covered by a grid and at each grid point, the differential equation is approximated by nodal values of the functions. This results in one algebraic equation per grid node in which the variable exact value at that point and a certain number of neighbour nodes are unknowns. The finite differences are not common for complex flow problem, while the method is very effective and suitable for structured grids.

- Finite Element method (FE): the domain is divided into a set of elements that can be approximated by triangles in a 2D case, while tetrahedra or hexahedra are used for 3D case. The equations are multiplied by a weight function before they are integrated over the domain. In the simplest FE method, the solution is approximated by a linear shape function in a way to guarantee continuity of the solution across element boundaries. The advantage of this method is that it can be applied to arbitrary geometries, the grids are easily refined and each element is subdivided. On the other side, the matrices of the linearized equations are not as well structured as those for regular grids, making it more difficult to find efficient solution methods.

- Finite Volume method (FV): it uses the integral form of the conservation equations previously described. The solution domain is subdivided into a finite number of contiguous control volumes (CVs), in which the equations are applied. At the centroid of each CV, there is a computational node in which the variable values are evaluated. Surface and volume integral are approximated using quadrature formulae, in order to obtain an algebraic equation for each CV, in which a number of neighbour nodal values appear. This method can be used for any type of grid and for complex geometries, so it is widely used in 3D CFD software.

1.4 Mesh in CONVERGE

The software automatically generates a perfectly orthogonal, structured grid at runtime based on user-defined grid control parameters [8]. This grid generation method completely eliminates the need to manually generate a grid. Runtime grid generation allows the grid to be changed during the simulation. Possible changes include scaling the cell size of the entire domain, locally refining or coarsening during the simulation, and adaptively refining the mesh. Another major advantage of runtime grid generation is the ability of CONVERGE to regenerate the grid near moving boundaries during the simulation without any input from the user.
The base grid size is the largest grid size available in the simulation, all other grid control strategies are specified with respect to the base grid size.

1.4.1 Fixed Embedding

The fixed embedding is used to refine the grid at specific locations in the domain where a finer resolution is critical to the accuracy of the solution. It is a useful tool for solving the flow problem in some part of the domain, for example in the combustion chamber near the spark plug or while simulating sprays by adding an area of fixed embedding by the nozzle to resolve the complex flow. Fixed embedding allows the rest of the grid to remain coarse to minimize the simulation time. CONVERGE also allows the user to specify the simulation starting and ending times of the fixed embedding This feature is important to reduce the computational time by turning on each fixed embedding only during critical simulation times. The *embed_scale* parameter, which must be a positive integer, scales the base grid sizes according to the following formula:

$$dx_{embed} = \frac{dx_{base}}{2^{embed\ scale}} \tag{10}$$

Different types of fixed embedding can be employed: a boundary embedding can be used when simulating flow around a valve (figure 2), to have extra resolution near the valve surface to more accurately model the flow in this section of the domain. For a moving surface (e.g., a valve), the embedding will move with the surface automatically. Sphere and cylinder embedding can be used to specify a spherical area or cylindrical area respectively (figure 3 and 4). Nozzle or injector embedding is used to refine the conical area around a nozzle and finally

a region embedding can be used for a grid refinement in an entire region, that can be for example the cylinder of an engine.

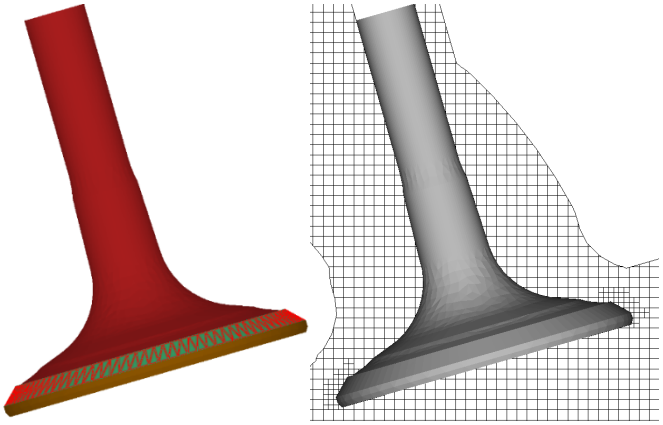

Figure 2: Boundary embedding used for a valve

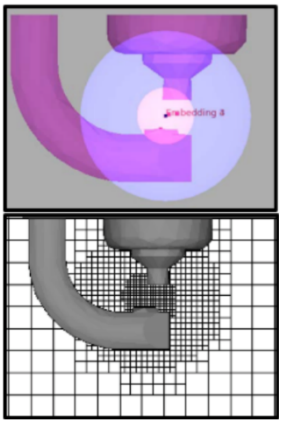

Figure 3: Sphere embedding for a spark plug

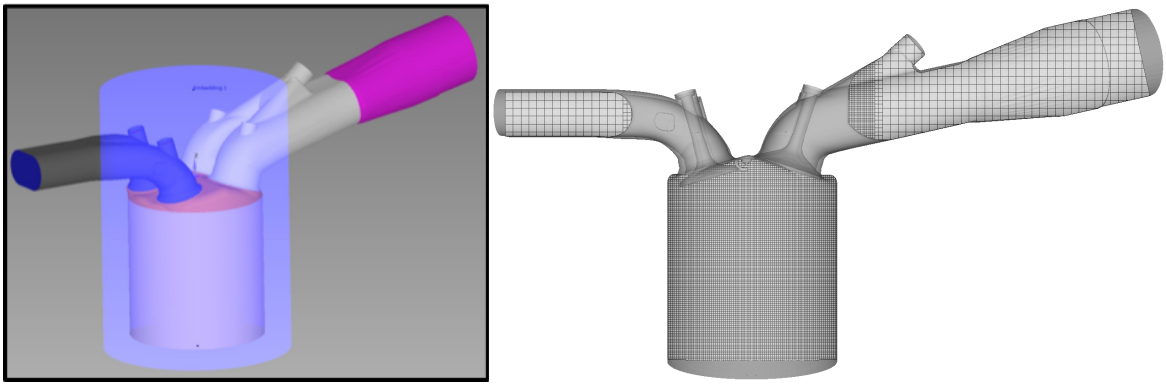

Figure 4: Cylinder embedding in ICE engines

1.4.2 Adaptive Mesh Refinement (AMR)

The Adaptive Mesh Refinement (AMR) is used to automatically refine the grid based on fluctuating and moving conditions such as temperature or velocity. This option is useful for using a highly refined grid to accurately simulate complex phenomena such as flame propagation or high-velocity flow without unnecessarily slowing the simulation with a globally refined grid. Ideally, a good AMR algorithm will add higher grid resolution (embedding) where the flow field is most under-resolved or where the sub-grid field is the largest (i.e., where the curvature or gradient of a specified field variable is the highest). The AMR method in

CONVERGE estimates the magnitude of the sub-grid field to determine where CONVERGE will add embedding. For a scalar, the sub-grid field is defined as the difference between the actual field and the resolved field:

$$\phi' = \phi - \bar{\phi} \tag{11}$$

Where:

ϕ is the actual field;

$\bar{\phi}$ is the resolved field;

ϕ' is the sub-grid field.

The sub-grid field can be expressed as an infinite series as in (23); but since it is not possible to evaluate the entire series, only the first term (the second-order term) in the series is used to approximate the scale of the sub-grid.

$$\phi' = -\alpha_{[k]} \frac{\partial^2 \bar{\phi}}{\partial x_k \partial x_k} + \frac{1}{2!} \alpha_{[k]} \alpha_{[k]} \frac{\partial^4 \phi}{\partial x_k \partial x_k \partial x_l \partial x_l} - \frac{1}{3!} \alpha_{[k]} \alpha_{[k]} \alpha_{[m]} \frac{\partial^6 \bar{\phi}}{\partial x_k \partial x_k \partial x_l \partial x_l \partial x_m \partial x_m} \tag{12}$$

Where:

$\alpha_{[k]} = dx_k^2/24$ for a rectangular cell;

AMR can be used for any or as many of the following fields: velocity, number of parcels per cell, temperature, void fraction, species, passives, or boundary (y+), with a different embedding scale and different sub-grid criterion for each condition. It is possible also to specify a maximum overall number of cells, in order to limit the number of embedded cells. If the number of cells in the grid reaches the maximum number, CONVERGE uses the AMR routine to determine where to put the embedding in a manner that best resolves the flow field and meets the maximum number of cells. To make optimal use of all of the cells when the cell limit is reached, CONVERGE will adjust the user-specified sub-grid value criteria as needed. That is, if there are too many cells, CONVERGE will increase the value of the user-specified sub-grid criteria. In figure 5 is represented an example of mesh in valve region that contains AMR, which automatically increases the grid resolution based on curvatures (second derivatives) in field variables.

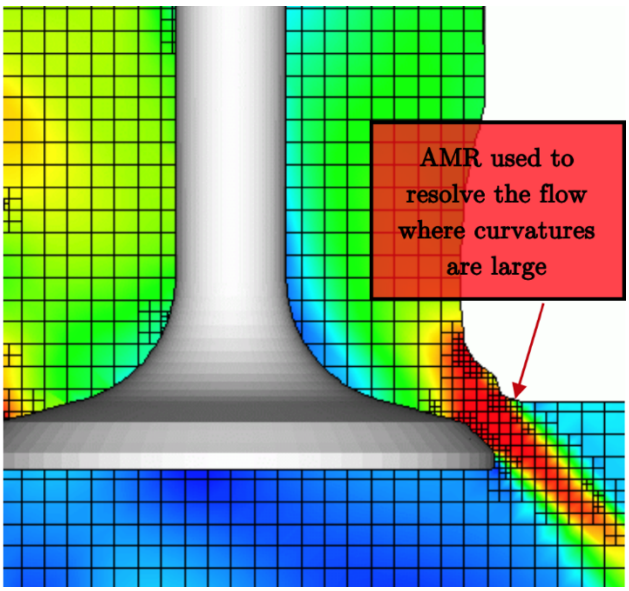

Figure 5: AMR to resolve the flow in valve region

1.5 Turbulence modelling

In engineering application, turbulent flows are prevalent: in the processing of liquids or gases with pumps, compressors, pipe lines the flows are generally turbulent, the flows around automobiles, airplanes, ships are turbulent; finally, the mixing of fuel and air in internal combustion engine takes place in turbulent flows. One of the most important features of turbulent flows is that the fluid velocity field varies significantly and irregularly in both position and time [9]. Moreover, the accurate and reliable modelling of turbulent flow is one of the most important challenges when dealing with this kind of engineering problems. It is important to underline that the velocity field is three-dimensional, time-dependent and random. Turbulence phenomena are characterized also by fluctuating vorticity: cross-section view of a turbulent flow typically appears as a diverse collection of streaks, strain regions, and swirls of various sizes that deform, coalesce, divide, and spin. Turbulence always involves a range of eddy sizes: the increase in the Reynold number leads to an increase in the size range. Besides the effects of turbulence that make it a prime importance phenomenon in many engineering applications, there is the effectiveness of transporting and mixing fluids. In fact, when different fluids are brought together to be mixed, it is generally desirable for this mixing to take place as rapidly as possible. Turbulence is also effective in mixing the momentum of a fluid; compared with

laminar flow, rates of heat and mass transfer at solid-fluid and liquid-gas interface are much enhanced in turbulent flows.

The most common methodologies used to model the turbulence consist of a set of partial differential equations, in some cases supplemented by algebraic equations that are solved numerically, for a given flow with appropriate boundary and initial conditions. Besides those methods, it is important to underline the following:

- Direct Numerical Simulation (DNS): it is the simplest approach and it gives also a great accuracy and high level of description. The method consists of solving the Navier-Stokes equations, with appropriate conditions for the considered flow, resolving all the scales of motion. Each simulation is a single realization of the flow. Moreover, it is important to underline that the computational cost is extremely high (increase as Re^3), limiting the application of the DNS method to flows characterized by low or moderate Reynolds numbers.

- Reynolds Averaged Navier-Stokes (RANS): the approach is based on the solution of Reynold equations to determine the mean velocity field. The Reynolds stresses, which appear in those equations, can be computed by a turbulence model, via the turbulent viscosity hypothesis or directly from modelled Reynolds-stress transport equations. RANS method will be better explained in the next section together with *k-ε model,* that is the approach used in the simulations performed in the thesis.

- Large Eddy Simulation (LES): in this method the equations are solved for a filtered velocity field that represents the larger-scale turbulent motions. There is also a model for the influence of smaller-scale motions that are not explicitly represented. LES is expected to be more accurate than RANS for flows in which large-scale unsteadiness is relevant. Its computational costs are high but, compared with DNS, the direct representation of small-scale motions is avoided.

The three approaches have different levels of resolution and modelling of the turbulent eddy scale, as can be appreciated from the figure 6.

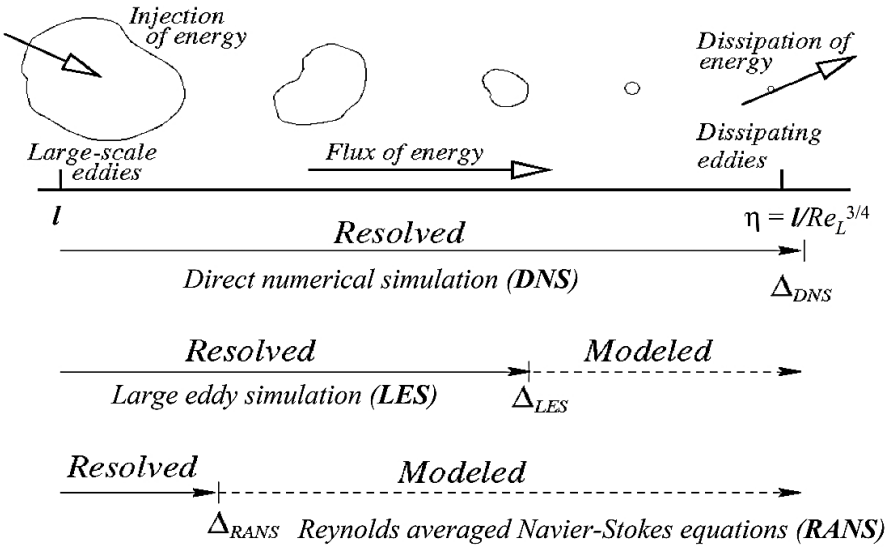

Figure 6: Level of resolution and modelling of turbulent scales for RANS, LES and DNS

As a comparison between the performances of the three approaches, in figure 7 an example of the RANS, LES and DNS prediction of a turbulent jet is presented.

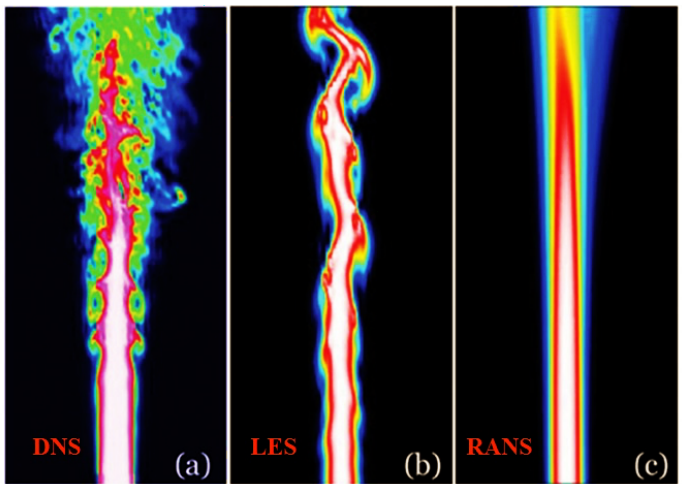

Figure 7: Turbulent jet predicted by DNS (a), LES (b), RANS (c) methods

1.5.1 RANS turbulence models

Reynolds Averaged Navier-Stokes models, as explained in the previous section, solve the equations for an ensemble-averaged velocity field and the magnitude of the turbulent fluctuations. In these models a flow variable, such as the velocity, is decomposed into an ensemble mean and a fluctuating term, as represented in figure 8 and explicitly in equation (10):

$$u(x,t) = \bar{u}(x,t) + u'(x,t) \tag{13}$$

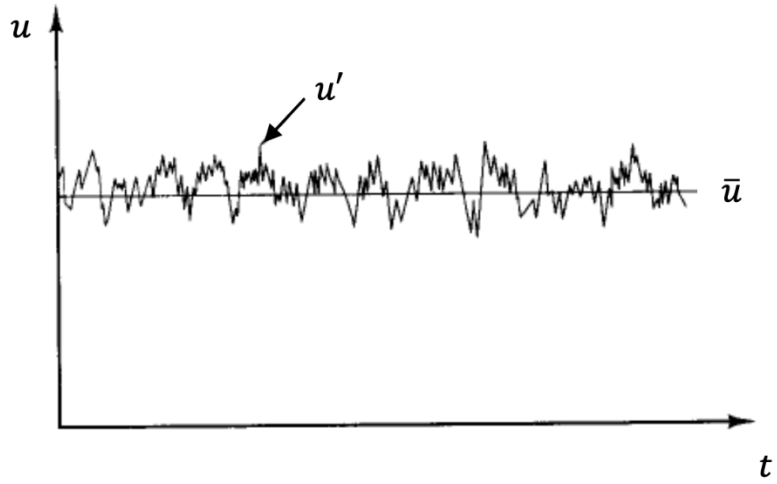

Figure 8: RANS decomposition of velocity field

Substituting the RANS decomposition into the continuity and momentum equations and averaging them, the system becomes in the case of an incompressible flow without body forces, for sake of simplicity, as follows:

$$\frac{\partial(\rho\bar{u}_i)}{\partial x_i} = 0 \tag{14}$$

$$\frac{\partial(\rho\bar{u}_i)}{\partial t} + \frac{\partial}{\partial x_j}\left(\rho\bar{u}_i\bar{u}_j + \rho\overline{u'_i u'_j}\right) = -\frac{\partial\bar{p}}{\partial x_i} + \frac{\partial\bar{\tau}_{ij}}{\partial x_j} \tag{15}$$

Where $\bar{\tau}_{ij}$ is the mean viscous stress tensor, expressed as:

$$\bar{\tau}_{ij} = \mu\left(\frac{\partial \bar{u}_i}{\partial x_j} + \frac{\partial \bar{u}_j}{\partial x_i}\right) \tag{16}$$

Dealing with the averaging of momentum equation is less simple, because of the non-linear convective term. In fact, the average of this non-linear quadratic term is equal to:

$$\overline{u_i u_j} = \overline{(\bar{u}_\iota + u'_\iota)(\bar{u}_j + u'_j)} = \bar{u}_i \bar{u}_j + \overline{u'_\iota u'_j} \tag{17}$$

The term $\rho\overline{u'_\iota u'_j}$ in equation (12), called Reynolds stresses, represents the effect of turbulence in the equation and need to be modelled in order to have the closure of the system.
RANS methods are based on the ***turbulent-viscosity hypothesis***, according to which the Reynolds stresses are given by:

$$\rho\overline{u'_i u'_j} = \mu_t\left(\frac{\partial \bar{u}_i}{\partial x_j} + \frac{\partial \bar{u}_j}{\partial x_i}\right) - \frac{2}{3}\rho\delta_{ij}k \tag{18}$$

The turbulent viscosity μ_t is expressed in different ways according to the RANS model used.

Standard and RNG k-ε Model

Between the most famous methods to model the Reynolds stresses there is the Standard k-ε model. It belongs to the class of two-equation models, in the sense that the transport equations are solved for two turbulence quantities: the turbulent kinetic energy k and the turbulent dissipation rate ε. In fact, the turbulent viscosity is expressed as a function of those two quantities:

$$\mu_t = C_\mu \rho \frac{k^2}{\varepsilon} \tag{19}$$

The turbulent kinetic energy is defined as:

$$k = \frac{1}{2}\overline{u'_i}\overline{u'_i} \tag{20}$$

The RNG k-ε model was developed using Re-Normalization Group (RNG) methods to renormalize the Navier-Stokes equations, in order to account for the effects of smaller scales of motion. In RNG theory the model constants are analytically derived.

The transport equation for the turbulent kinetic energy, equal between the two methods, is given by:

$$\frac{\partial \rho k}{\partial t} + \frac{\partial \rho u_i k}{\partial x_i} = \tau_{ij} \frac{\partial u_i}{\partial x_j} + \frac{\partial}{\partial x_j}\left(\frac{\mu + \mu_t}{Pr_k}\right)\frac{\partial k}{\partial x_j} - \rho\varepsilon + \frac{C_s}{1.5} + S_s \tag{21}$$

The transport equation for the dissipation of turbulent kinetic energy is given by:

$$\frac{\partial \rho \varepsilon}{\partial t} + \frac{\partial \rho u_i \varepsilon}{\partial x_i} = \frac{\partial}{\partial x_i}\left(\frac{\mu}{Pr_k}\frac{\partial \varepsilon}{\partial x_j}\right) + c_{\varepsilon 3}\rho\varepsilon\frac{\partial u_i}{\partial x_i} + \left(c_{\varepsilon 1}\frac{\partial u_i}{\partial x_j}\tau_{ij} - c_{\varepsilon 2}\rho\varepsilon + C_s S_s\right)\frac{\varepsilon}{k} + S - \rho R \tag{22}$$

where S is the user-supplied source term and S_S is the source term that represents interactions with discrete phase (spray). The $c_{\varepsilon i}$ terms are model constants that account for compression and expansion. In the previous equation, R = 0 for the standard k- model, while in RNG k-ε model it is equal to:

$$R = \frac{C_\mu \eta^3 (1 - \eta/\eta_0)\varepsilon^2}{(1 + \beta\eta^3)k} \tag{23}$$

1.6 Combustion modelling

1.6.1 Turbulent premixed combustion

In a conventional spark-ignition engine the fuel and air are mixed together in the intake system and then, through the intake valve, introduced into the chamber where they are mixed with residual gases and then compressed. Combustion is initiated towards the end of compression stroke by an electric discharge at the spark plug. A turbulent flame develops, propagates

through the premixed mixture of fuel, air and burned gas, until it reaches the combustion chamber walls and extinguishes [10].

The structure of a premixed flame consists of three zones (figure 9):

- Preheat zone: where the temperature of unburned gas is raised by the heat transfer from chemical reaction zone and no major reaction or energy release takes place;

- Oxidation layer: the layer at the interface with burned gas, where chain breaking reactions take place and the temperature reaches its maximum;

- Inner layer: this region is located between the previous two, where the chain branching reactions take place and the temperature gradient is maximum. It represents the part responsible for keeping the combustion alive. The inner layer is also sensitive to the turbulence: if the smaller eddies penetrate into the layer, thus enhancing the convective heat exchange, it can lead to the extinction of the flame.

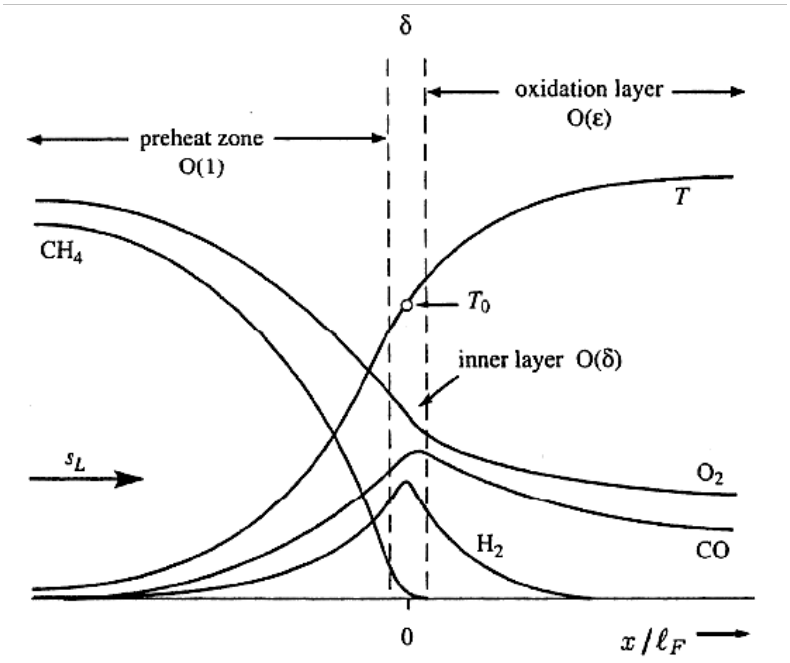

Figure 9: Structure of a typical premixed flame

1.6.2 Combustion regimes

Turbulent combustion involves various lengths, velocity and time scales describing turbulent flow field and chemical reactions. In order to understand the influence of the turbulence on the premixed combustion, the analysis is based on the comparison between these scales. The Damköhler number compares the turbulent (τ_t) and the chemical (τ_c) time scales:

$$Da = \frac{\tau_t}{\tau_c} = \frac{L_t}{\delta_l} \cdot \frac{S_L}{u'} \tag{24}$$

Remembering that for turbulent premixed flames, the chemical time scale may be estimated as the ratio of the thickness (δ_l) and the propagation speed of the laminar flame (S_L), while the turbulent time is calculated as the ratio between the turbulent integral scale (L_t) and the root mean square (RMS) value of the turbulent velocity (u').

For large values of the Damköhler number ($Da>>1$) chemical time is short compared to the turbulent one, corresponding to a thin reaction zone distorted and convected by the flow field. The internal structure of the flame is not strongly affected by turbulence and may be described as a laminar flame element called a ‘flamelet'. The turbulent structures wrinkle and strain the flame surface. On the other hand, a low Damköhler number ($Da<<1$) corresponds to a slow chemical reaction. Moreover, reactants and products are mixed by turbulent structures before reaction.

The Karlovitz number, instead, is the ratio between chemical time scale and turbulent time scale of the smallest eddies (Kolmogorov scale):

$$Ka = \frac{\tau_c}{\tau_k} = \frac{\delta_l}{L_k} \cdot \frac{u_k}{S_L} \tag{25}$$

The Karlovitz number is used to define the *Klimov-Williams criterion*, corresponding to $Ka<1$, which separates two combustion regimes. This criterion was first interpreted as the transition between the flamelet regime previously described and the distributed combustion regime, where the flame inner structure is strongly modified by turbulence motions. For Karlovitz numbers larger than unity, turbulent motions become able to affect the flame inner structure but not necessarily the reaction zone.

According to Karlovitz number, the following subdivision can be proposed [11]:

a) *Ka<1:* ***Flamelet regime or thin wrinkled flame regime***. In this situation the inner structure of the flame in not affected by turbulence that can only strain the flame surface, as previously described (Figure 10a). A further classification can be made based on the velocity ratio:

- $u'/S_L < 1$: ***Wrinkled flame***, in which laminar propagation is predominant and the interactions between turbulence and combustion remain limited.

- $u'/S_L > 1$: ***Wrinkled flame with pockets or 'corrugated flames'***, in which larger structure become able to induce flame front interaction leading to pockets.

b) *1<Ka<100:* ***Thickened wrinkled flame regime or thin reaction zone***. The turbulent motions are able to affect and to thicken the flame preheat zone but not the reaction zone which remains close to a laminar reaction zone (Figure 10b).

c) *Ka>100:* ***Thickened flame regime or broken reaction zone***. In this case preheat and reaction zone are both strongly affected by turbulent motions and no laminar flame structure can be identified (Figure 10c).

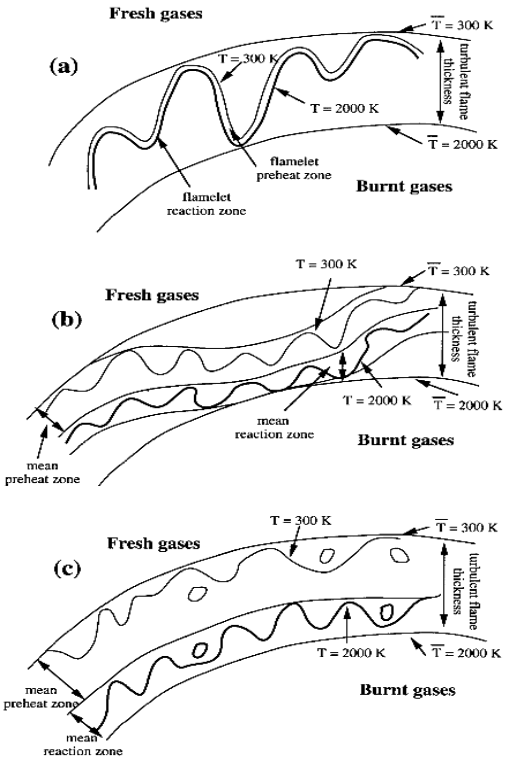

Figure 10: a) Flamelet regime; b) Thin reaction zone; c) Broken reaction zone

The classification can be better appreciated on the combustion regime diagram or *Borghi plot* (Figure 11) in which on the x and y axis are reported respectively the length scale ratio (L_t/δ_l) and the velocity ratio (u'/S_L).

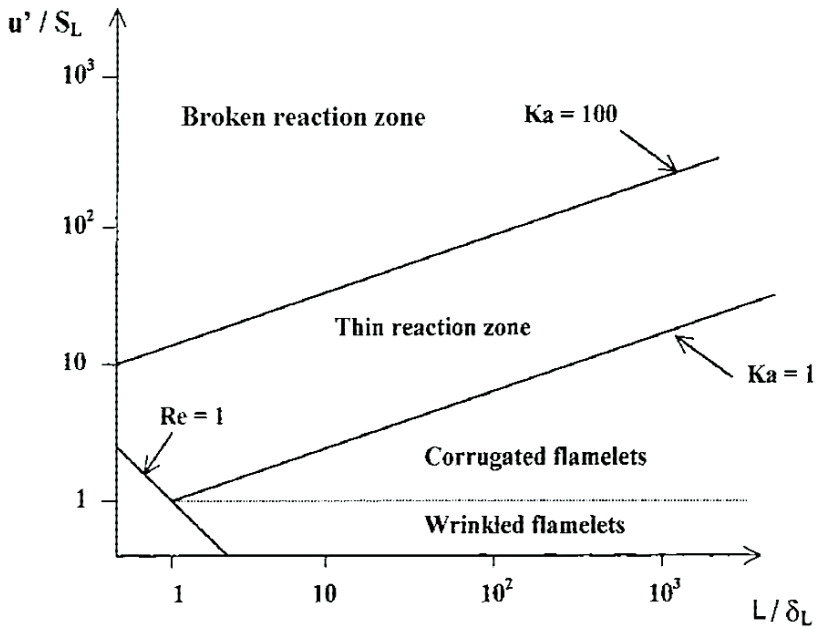

Figure 11: Combustion regime diagam or "Borghi plot"

1.6.3 Laminar Flame Speed

The laminar flame speed is an important intrinsic property of a mixture of fuel, air and burned gas. It is defined as the velocity, relative to and normal to the flame front, with which unburned gas moves into the front and is transformed into products under laminar flow conditions. Laminar flame speed is usually are usually measured in spherical close vessel, by propagating a laminar flame radially outward from the vessel center. The velocity can be expressed as:

$$S_L = \frac{dm_b/dt}{A_f \rho_u} \tag{26}$$

Where:

dm_b/dt is the mass burning rate;

A_f is the flame area;

ρ_u is the density of unburned gas.

The laminar flame speed is a fundamental property of fuels, resulting from the combined influences of diffusivity, exothermicity, and reactivity. It is a key parameter to describe complex combustion phenomena such as flame stabilization, extinction, turbulent flame structure and velocity. LFS is influenced by some operating parameters such as pressure temperature, equivalence ratio, but also the quantity of exhausted gas re-introduced in the chamber (EGR). In particular, values of laminar flame speed for different fuels, in function of equivalence ratio are represented in figure 12. It can be noticed that the maximum speed is reached in a slightly rich zone.

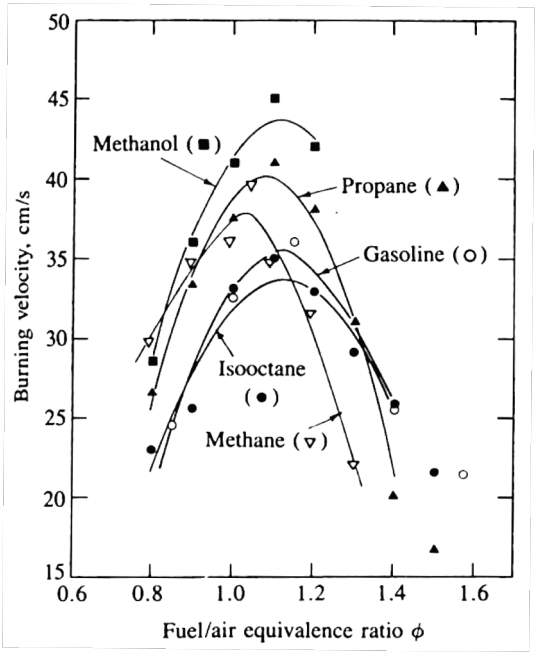

Figure 12: Values of laminar flame speed for different fuels

The correlation of laminar flame speed as a function of temperature and pressure is necessary for the CFD simulation. In fact, a chemical mechanism is a theoretical conjecture that tries to describe what takes place at each stage of an overall chemical reaction because the detailed steps of a reaction are not observable in most cases. In internal combustion engines, the kinetic mechanisms are used to model the combustion process that takes places, in order to predict some important features of fuels used, such as the laminar flame speed, ignition delay time and pollution formation. In the simulation part of the thesis work, the LFS table obtained by [12] are implemented in CONVERGE CFD software through user-defined function (UDF). The tables were obtained with DARS software, simulating the kinetic mechanism GRI Mech 3.0, that is one of the most widely used mechanisms for natural gas.

1.6.4 Extended Coherent Flame Model (ECFM)

The combustion model used in the thesis work is the ECFM model, that belongs to the class of premixed combustion formulations. ECFM is an extension of Coherent Flame Model (CFM), that is a combustion model adapted to the *flamelet* regime. This modeling is particularly suited to the description of premixed flame combustion, which represents the main oxidation mechanism in spark ignition engines. It supposes that the chemical reaction of fuel oxidation

occurs in a very thin layer. In premixed combustion, this layer separates burned and unburned gases and propagates toward the fresh mixture of fuel, oxygen and dilutant. The principal idea on which the model is based consists in describing locally the fuel/air (F/A) equivalence ratio in fresh gases, composition (including residual gases) and temperature, allowing to improve the description of large-scale burned/unburned stratification [13].

The ECFM model allows the simulation of the two premixed combustion modes, premixed propagation flame combustion (PF) in SI engines as well as knock (AI) and pollutant formation, even in highly stratified cases. Based on this model, the unified Diesel/gasoline combustion model ECFM3Z was developed [14]. In this model, the unburned/burned gas zones description of the ECFM model is kept, as well as the premixed flame description based on the flame surface density equation. In order to account for diffusion flame (DF) and mixing processes, each computational cell is split into three mixing zones: a pure fuel zone, a pure air plus possible residual gases (EGR) zone and a mixed zone, as schematically presented in Figure 13. This structure allows to account for the three main combustion modes (AI, PF and DF) encountered in most combustion devices.

As combustion can obviously not take place in regions *A* and *F*, it is only considered possible in region *M*. Combustion calculations are thus conditioned in this zone according to the description directly taken from the ECFM model. In the model are considered two possible states for gases during combustion: the unburned gas zone and the burned gas zone corresponding to superscripts *u* and *b* in Figure 13. The amount of unburned/burned gases in the mixed zone M is given by the progress variable *c* which is equal to zero when the burned gas mass is zero, and equal to one when the total mass contained in the mixed zone has been burned. Burned gases of region M^b have a temperature T^b while the gases of the five other regions have the same temperature T^u. Therefore, even if regions F^b and A^b have the same superscript *b*, they do not correspond to burned gases but rather to unburned gases which will mix in region M^b.

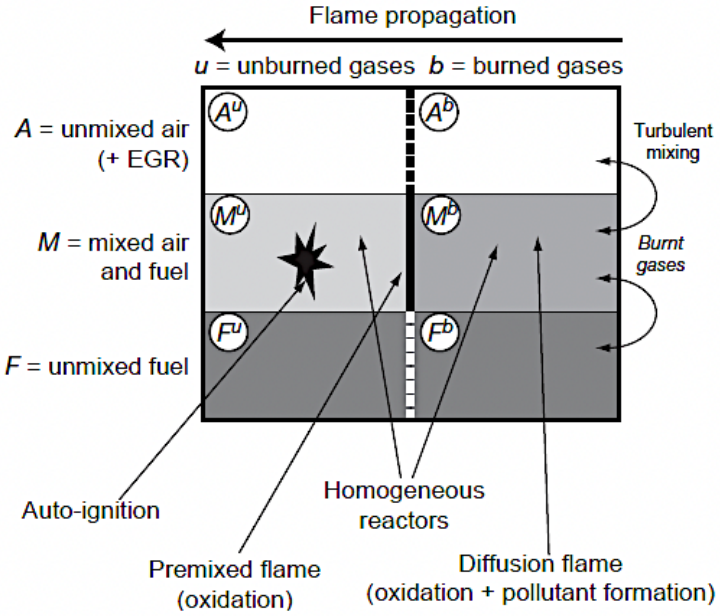

Figure 13: Scheme of ECFM model

The flame surface density transport equation is:

$$\frac{\partial \Sigma}{\partial t} + \frac{\partial u_j \Sigma}{\partial x_i} = \frac{\partial}{\partial x_i}\left(\frac{\mu}{Sc}\frac{\partial(\Sigma/\bar{\rho})}{\partial x_i}\right) + (P_1 + P_2 + P_3)\Sigma - D + P_k \qquad (27)$$

Where:

- Sc is the Schmidt number;
- $P_1 = \alpha K_t$ is the flame surface density production by turbulent stretch and α is a calibration parameter (constant for turbulent stretch);
- P_2 takes into account the effect of the flame thermal expansion and curvature;
- P_3 represents the production by the mean flow dilation;
- D is a destruction term due to consumption;
- P_k is the source term (such as a spark plug).

1.6.5 Imposed Stretch Spark Ignition Model (ISSIM)

The ISSIM model can be coupled with the ECFM combustion model, with the main purpose of simulating the reaction rate due to the flame surface density (FSD) starting at the moment of ignition. This model simultaneously represents both the electrical circuit energy deposition and the flame surface and mass deposition. The ISSIM model derives directly from the ATKIM spark ignition model, whose electrical circuit scheme is represented in figure 14. The primary circuit includes the battery and the primary inductance. In particular, when the switch is open, the energy is stored in the primary inductance [8].

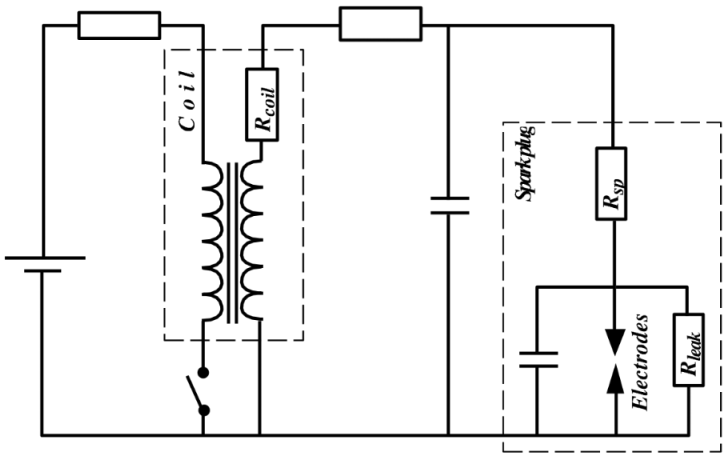

Figure 14: ATKIM electrical circuit scheme

The energy stored in the primary inductance L_p of the circuit is equal to:

$$E_{mag,prime} = \frac{1}{2} L_p i_p^2 \tag{28}$$

Approximately 60% of the energy is transferred to the spark plug, while the remaining energy is dissipated by the secondary inductance. The ISSIM considers only the secondary part of the inductive ignition system. The life of the spark is generally divided into three phases. The breakdown and arc phases, which last typically less than a microsecond, are taken into account by considering an instantaneous energy deposit in the gas, E_{bd}, given by:

$$E_{bd} = \frac{V_{bd}^2}{C_{bd}^2 d_{ie}} \tag{29}$$

Where:

V_{bd} is the breakdown voltage;

C_{bd} is a constant;

d_{ie} is the inter-electrode distance (specified by the user).

Then there is the glow phase, which can last a few milliseconds; the current discharged by the spark plug can be expressed as:

$$i_s = \sqrt{\frac{2E_s}{L_s}} \tag{30}$$

Where the inductance L_s is specified by the user and E_s is the electrical energy available on the secondary circuit is given by. The glow phase lasts until the energy $E_s(t)$ is positive.

$$\frac{\partial E_s(t)}{\partial t} = -R_s i_s^2(t) - V_{ie} i_s(t) \tag{31}$$

As the spark voltage reaches the breakdown voltage ($V_{ie} > V_{bd}$), the gas starts to break down and the conductive phase begins. Once the conductive phase has begun, the gas starts to receive energy from the spark kernel. The energy received must be greater than a critical value in order to have a proper ignition of the gasses. Then the spark is stretched by convection and turbulent motion of the flow. When ignition begins, a mass of burning gases is deposited near the spark. In the ISSIM model, based on experimental observation, the initial kernel size does not depend on the mixture composition but rather scales with the deposited electrical energy. The target burned gas volume fraction is given by:

$$\bar{c}_{ign}(x, t_{ign}) = c_0 \, exp\left(-\left(\frac{|x - x_{spk}|}{0.5 d_{ie}}\right)^2\right) \tag{32}$$

Where x gives the coordinates of the cell and x_{spk} is the spark plug location.

The ignition flame surface density (FSD) source is introduced at the start of ignition. As suggested by experiments, the initial flame kernel is assumed to be a sphere and its radius is equal to:

$$r_b^{ign} = \left(\frac{3}{4\pi}\int \bar{c}_{ign}\, dV\right)^{1/3} \tag{33}$$

The FSD is defined as:

$$\Sigma_{ign} = C_{surf}\frac{3\bar{c}}{r_b^{ign}} \tag{34}$$

where C_{surf} is a user-specified calibration parameter, that corresponds to an initial wrinkling value, allowing to account for the non-perfect sphericity of the flame kernel.

2. CFD Model and Simulations

In the present section the procedure followed in the practical part of the thesis work will be explained in detail. The starting point for the simulation is the experimental data, from the engine specifications used in the 3D model to the engine major quantities recorded, which are used for the validation of the model. The model setting and the simulation setup is then shown. The model is then validated with the experimental data and used to predict the behavior of the engine in the case of diluted combustion (EGR). Finally, a discussion about the results of the simulation and a comparison between the different cases investigated. the working point of the engine that is studied in the simulation part is 3000rpm x 8 bar. The simulations performed include the stoichiometric condition and the lean condition, for which the model has to be validated with experimental data. For the stoichiometric condition the model is then used to predict the behavior of the engine with EGR dilution.

2.1 Experimental Data

The engine used for the simulations is a *Fiat FIRE 1.4 16V Turbo CNG*, which is installed in the Energy department laboratory. The engine, whose layout is in figure 15, will be referred as *Polito* engine from now on. The main specifications are listed in table 1.

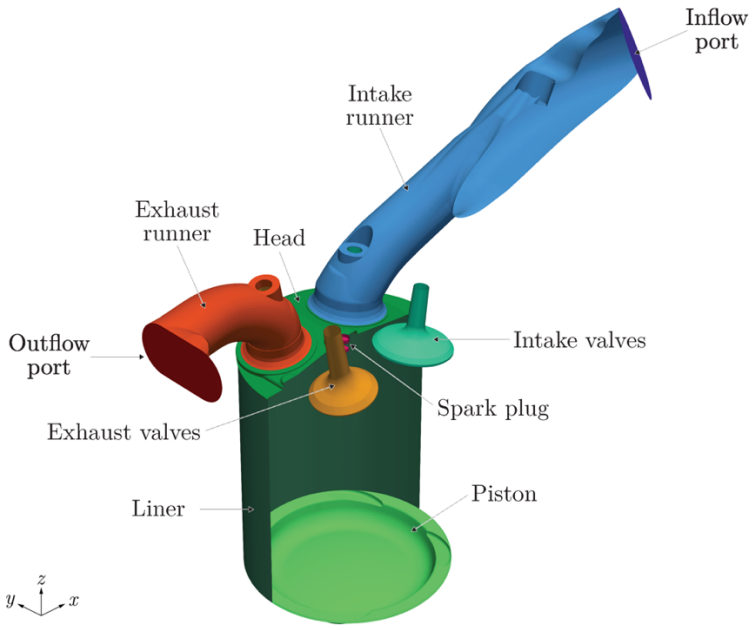

Figure 15: Layout of Polito engine

Engine Specification

Bore	72.0 mm
Stroke	84.0 mm
Compression ratio	9.8
Cylinder number	4
Displacement	1367 cm^3
Valves per cylinder	4
Intake valve	Opening duration: 250 CAD / max lift: 7 mm
Exhaust valve	Opening duration: 244 CAD / max lift: 7 mm
Combustion chamber	Pent-roof
Turbocharger	WG-controlled FGT
Intercooler type	Water-to-air
Injection	Port fuel

Table 1: Specifications of Polito engine

The engine has been operated on a test bench installed in an engine hall for dynamometer experiments. The test rig is equipped with a hot-film air-mass sensor in the intake system, two air–fuel ratio UEGO sensors (dedicated to the rich mixtures and to the lean mixtures fields, respectively) in the exhaust system, a pressure sensor in the injection rail as well as with several thermocouples for the measure of the temperatures of the intake flow, of the fuel and of the exhaust gases [13]. Four water-cooled piezoelectric transducers are installed on the engine cylinders head to detect the pressure time-histories in the four combustion chambers, thus allowing for a thorough investigation into the cylinder-to-cylinder variation. The engine speed has been measured by means of a crankshaft driven encoder which was also generating the time base for the acquisition system. The test facility includes an upgraded multipurpose exhaust-gas analyzer capable of measuring the levels of THC, MHC, NO_x, CO, CO_2 and O_2 in the exhaust gases for gasoline, diesel or alternative fuel (such as LPG and CNG) operations. All the measuring instruments were connected to a PC based 'National Instruments' data acquisition system allowing for the simultaneous acquisition of the major engine working quantities. A high-frequency acquisition card enabled measurements of the in-cylinder pressure time-history to be recorded over the whole engine cycle. The engine has been tested with different amounts of hydrogen added to natural gas (0%, 15% and 25% by volume) and the ECU control parameters have in time properly been adjusted to meet the hydrogen/methane blend

requirements. The CNG and HCNG blends composition and main average properties are reported in Table 2. Natural gas and HCNG have been safely stored at a pressure of 180 bar in a dedicated room located outside the building hosting the engine test rig. The mixture was delivered through stainless steel pipes from the tanks to the pressure reducer ahead of the injection system.

Composition (volume fraction)	**CNG**	**HCNG15**	**HCNG25**
Methane	≥98	≥83.3	≥73.5
Ethane	≤1	≤0.85	≤0.75
Butane	≤0.6	≤0.51	≤0.45
Carbon dioxide	≤1	≤0.85	≤0.85
Hydrogen	0	15 ± 2	25 ± 2
Average properties			
α_{st}	17.05	17.40	17.70
LHV [MJ/Kg]	49.1	53.7	54.6
MN	≈99	≈84	≈74

Table 2: Composition and average properties of CNG and HCNG blends

2.2 Simulation Setup

2.2.1 Numerical and Physical models

The model is implemented in CONVERGE CFD software starting from the geometry of the engine. The numerical setup for the solution of the fluid-dynamic problem and the physical models used for turbulence and combustion, that has been discussed in previous sections, are shown in table 3.

Numerical Setup

Flow	Compressible
Gas simulation	Redlich-Kwong model
Numerical method	Implicit method
Turbulence model	RNG k-ε
Combustion model	ECFM
Ignition model	ISSIM
Heat transfer model	Han & Reitz

Table 3: Numerical setup used in the simulations

2.2.2 Mesh Setting

The base grid chosen for the simulations performed as well as the mesh refinement setting are shown in table 4. The two techniques previously described, AMR and the Fixed Embedding, are used to refine the mesh where there is a need for higher accuracy of the solution, such as the cylinder region or the spark plug area, or to resolve the flow where the gradient of velocity or temperature fields are above a limit value. A view of the mesh inside the domain is given in figure 16.

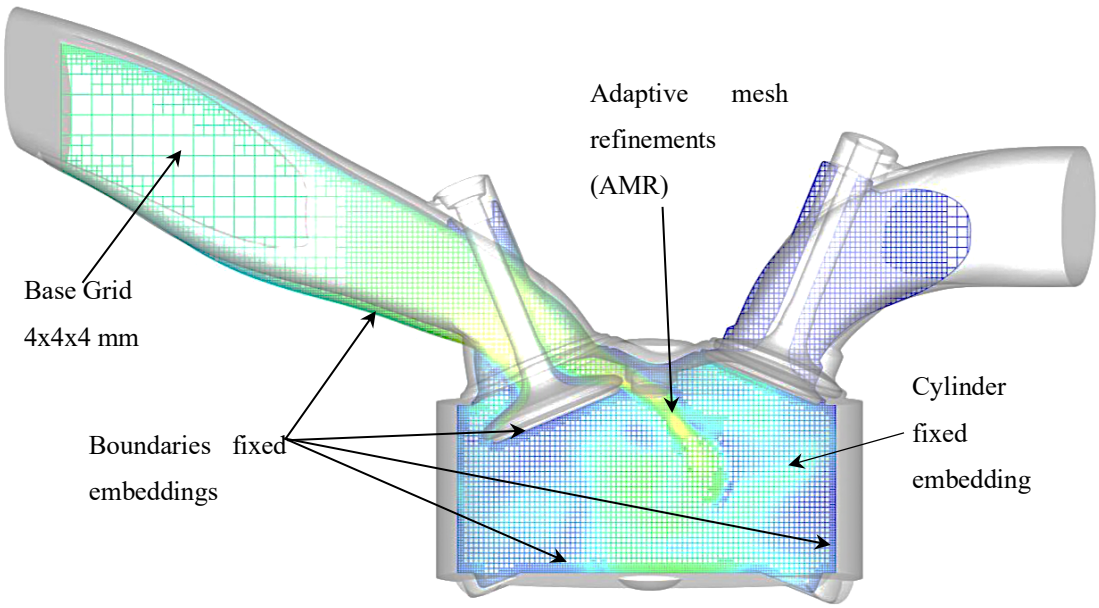

Figure 16: Mesh used in the model

Mesh Setting	
Base grid	4 x 4 x 4 [mm]
Fixed Embedding (cylinder)	Embedded type: region / Scale=1
Fixed Embedding (head, liner, piston)	Embedded type: boundary / Scale=2
Fixed Embedding (intake valve)	Embedded type: boundary / Scale=2
Fixed Embedding (intake valve angle)	Embedded type: boundary / Scale=3
Fixed Embedding (exhaust valve)	Embedded type: boundary / Scale=1
Fixed Embedding (exhaust valve bottom)	Embedded type: boundary / Scale=2
Fixed Embedding (spark plug)	Embedded type: sphere / Scale=4
Fixed Embedding (spark plug layer)	Embedded type: boundary / Scale=2
Fixed Embedding (intake port)	Embedded type: boundary / Scale=2
Fixed Embedding (exhaust port)	Embedded type: boundary / Scale=1
AMR – velocity (cylinder)	Sub-grid criterion= 1 [m/s] / Scale=3
AMR – temperature (cylinder)	Sub-grid criterion= 5 [K] / Scale=3
AMR – velocity (intake)	Sub-grid criterion= 1 [m/s] / Scale=3
AMR – temperature (intake)	Sub-grid criterion= 2 [K] / Scale=3
AMR – velocity (exhaust)	Sub-grid criterion= 1 [m/s] / Scale=3
AMR – temperature (exhaust)	Sub-grid criterion= 8 [K] / Scale=3

Table 4: Mesh setting used in the simulations

2.2.3 Initial & Boundary condition

The initial and boundary condition for the solution of fluid dynamic and temperature problem are assigned following the experimental data. The scheme of the different conditions applied to the domain is in figure 17.

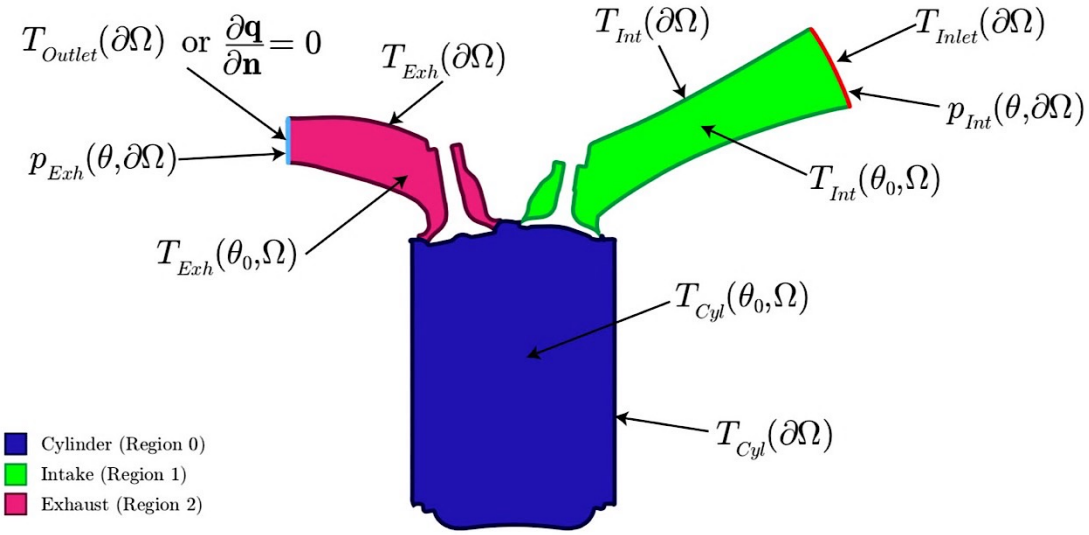

Figure 17: Initial and Boundary conditions

The domain is divided in three different regions: cylinder, intake and exhaust. The simulated cycle starts from 180° CAD in the exhaust phase of the working cycle of the engine, so the cylinder and exhaust region are at the same pressure and temperature initial condition. This choice also allows easier modelling of exhaust residual gas in the clearance at the beginning of intake phase. The initial and boundary conditions values are summarized in table 5.

Initial/Boundary Conditions

$T_{cyl}(\theta_0,\Omega)$	≈ 950 K
$T_{int}(\theta_0,\Omega)$	≈ 300 K
$T_{exh}(\theta_0,\Omega)$	≈ 950 K
$T_{inlet}(\partial\Omega)$	≈ 300 K
$T_{cyl}(\partial\Omega)$	≈ 600 K
$T_{int}(\partial\Omega)$	≈ 450 K
$T_{exh}(\partial\Omega)$	≈ 650 K
p_{int}	Profile from experiments
p_{exh}	Profile from experiments

Table 5: Initial and Boundary conditions values

2.3 Validation of the model

Once the CFD model has been developed, the simulations can be performed. The model has to be validated with experimental data first. The experiments include the tests of the three different fuels (pure CNG, and the two blends HCNG15 and HCNG25) without EGR. The procedure adopted in the validation process is to calibrate the model for the case of HCNG15 without EGR, using the relative LFS table. The first set of simulations to be run has the objective to find the perfect combination of the two calibration parameters: *wrinkling factor (C_{surf}) and turbulent stretch coefficient (α)* that allow the pressure inside the chamber to match the experimental one. Then, keeping the calibration parameters constant, the model is used to simulate the case of pure CNG and HCNG25 just by changing the LFS table. If the results match the experimental data, the validation process is completed, and the model can be used to predict the EGR cases. A scheme of the procedure is shown in Figure 18.

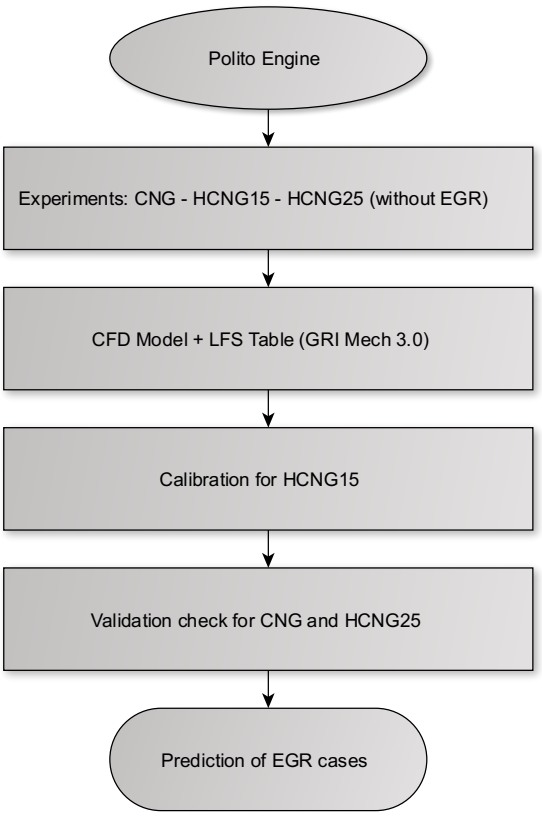

Figure 18: Scheme of the validation process

2.3.1 Calibration

The two calibration parameters have to be tuned properly in order to match the experimental in-cylinder pressure curve. They affect the combustion and heat release part of the cycle, in particular:

Effect of wrinkling factor (C_{surf})

This parameter concerns the wrinkling of the flame kernel, increasing the area through which the flame propagates, the higher will be the peak firing pressure. The effect of this parameter is taken into account in the ignition phase, hence the increased pressure that can be observed to be in the whole combustion phase, is only due to the boosting effect of the very first part after the spark discharge. In figure 19 there is represented the influence of wrinkling factor on in-cylinder pressure, while in figure 20 there is the effect on heat release curve. It is noticeable that the pressure curve is shifted upward and leftward with increased C_{surf} while the heat release curve is shifted leftward and the slope remains more or less the same.

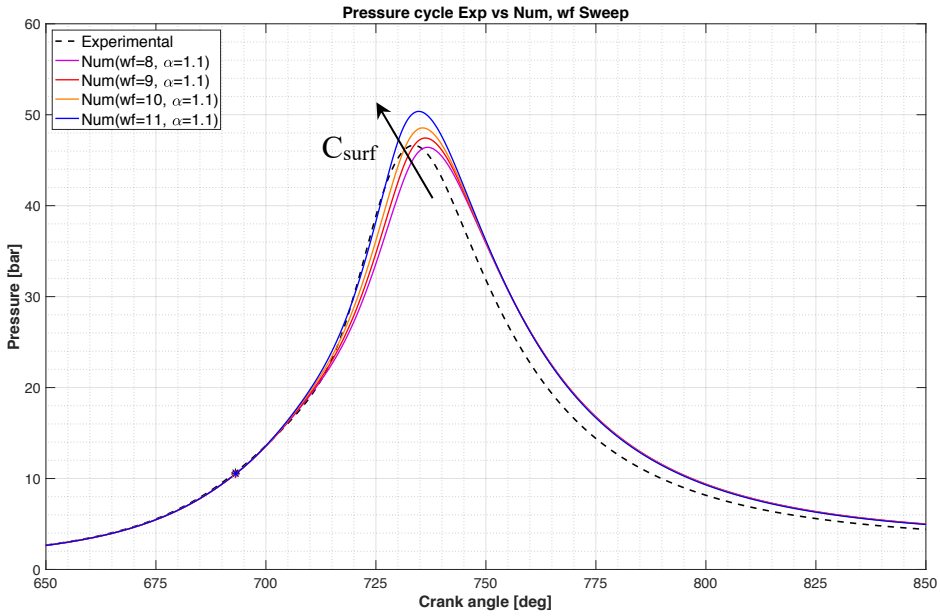

Figure 19: Effect of wrinkling factor on pressure cycle

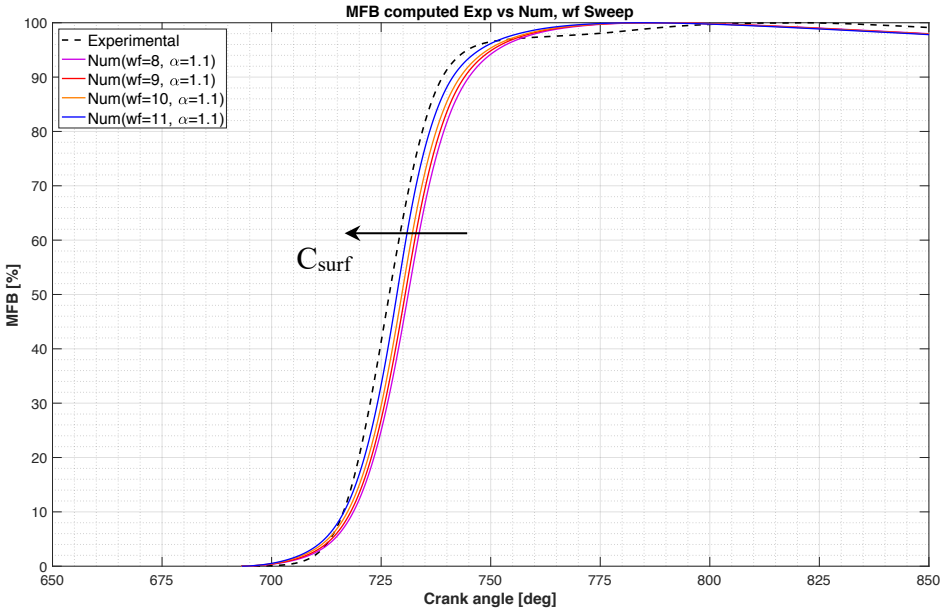

Figure 20: Effect of wrinkling factor on heat release curve

Effect of turbulent stretch coefficient (α)

This parameter affects the combustion phase because it is a multiplying coefficient in the transport equation of the flame surface density. Increasing the value of α, the higher the pressure in the combustion phase will be. The effect of turbulent stretch on pressure cycle and on heat release are shown in figure 21 and 22. It can be noticed that, by increasing α, the pressure curve is shifted upward. For what concerns the heat release, by increasing α, the curve becomes steeper, while the first part remains almost the same.

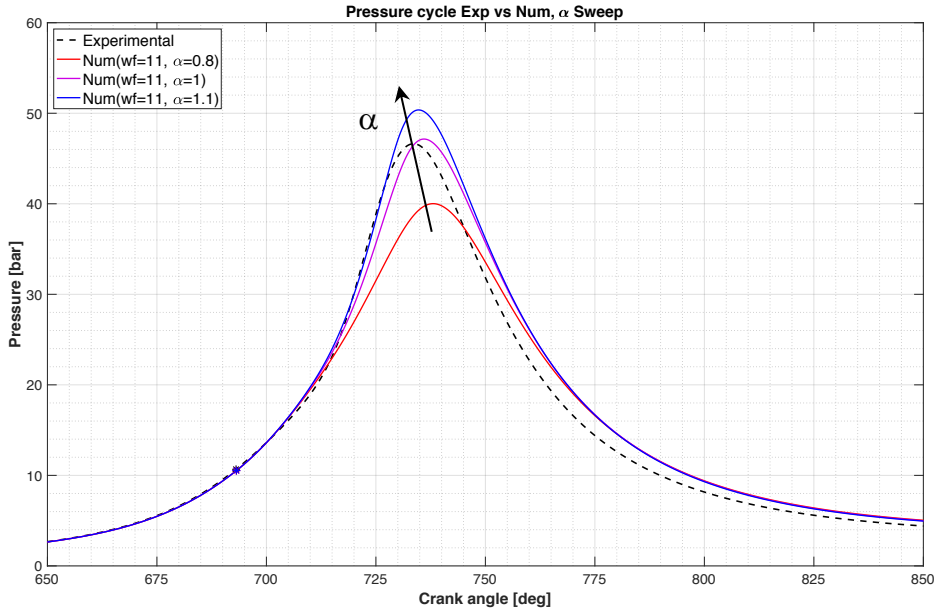

Figure 21: Effect of turbulent stretch factor on pressure cycle

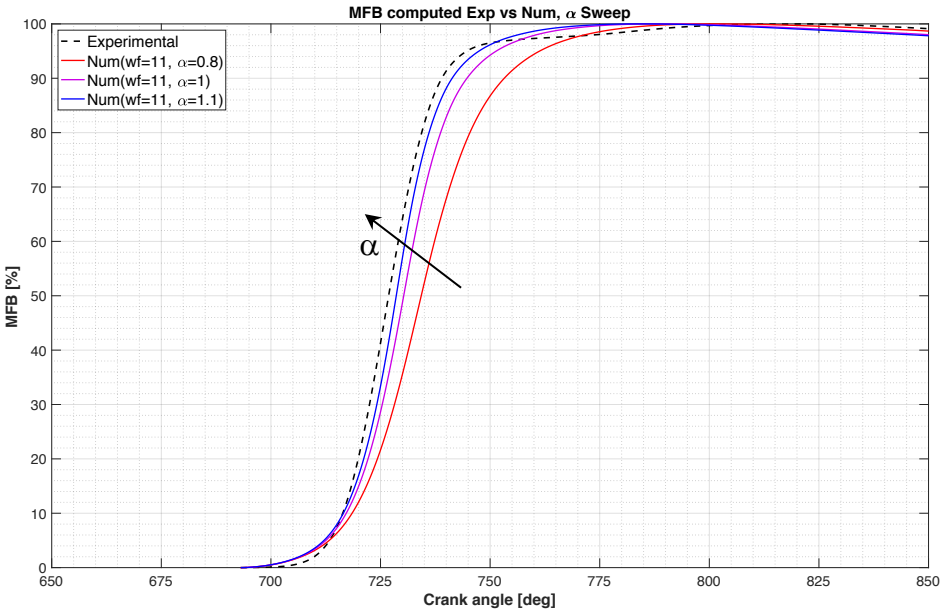

Figure 22: Effect of turbulent stretch factor on heat release curve

2.3.2 Stoichiometric combustion λ=1

The calibration parameters chosen are:

$$\begin{cases} C_{surf} = 11 \\ \alpha = 1 \end{cases}$$

The results of the validation for stoichiometric combustion are presented in the following. In Figure 23 the comparison between the in-cylinder pressure time-history of the numerical and experimental cycles, in the case of HCNG15 EGR0% is represented. In Figure 24 there is the comparison between the burned mass fraction (MFB) of the two datasets, computed by a first law heat release model [16], which gives an indication of the heat release rate in the combustion process.

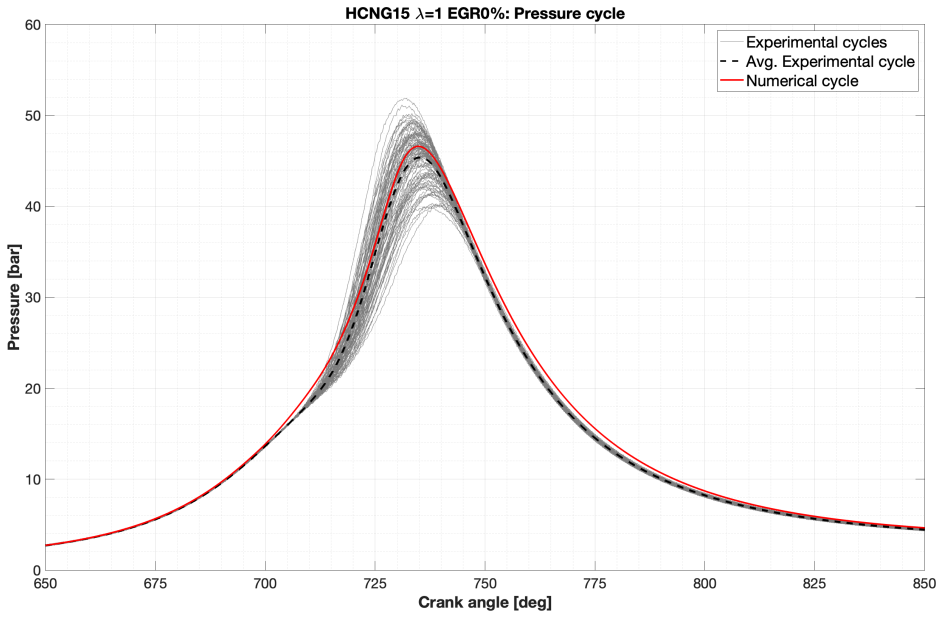

Figure 23: In-cylinder pressure time history of numerical and experimental cycles for HCNG15 λ=1

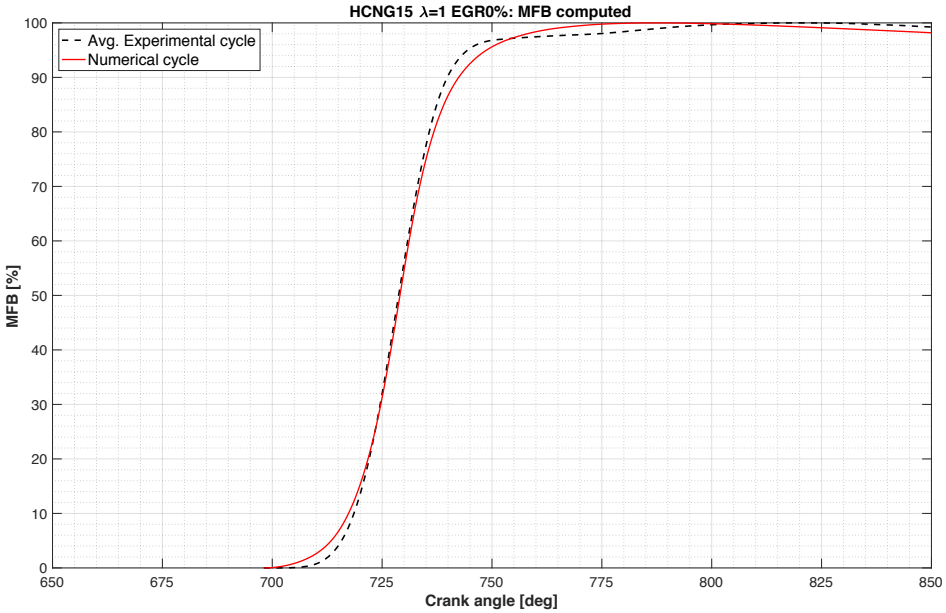

Figure 24: MFB computed of numerical and experimental cycles for HCNG15 λ=1

As can be seen in the picture, the pressure inside the cylinder matches perfectly the experimental data and also the heat release is well reproduced. The same comparisons, for pressure cycles and MFB computed, are shown for CNG EGR0% in Figure 25 and 26, while for HCNG25 EGR0% are shown in Figure 27 and 28.

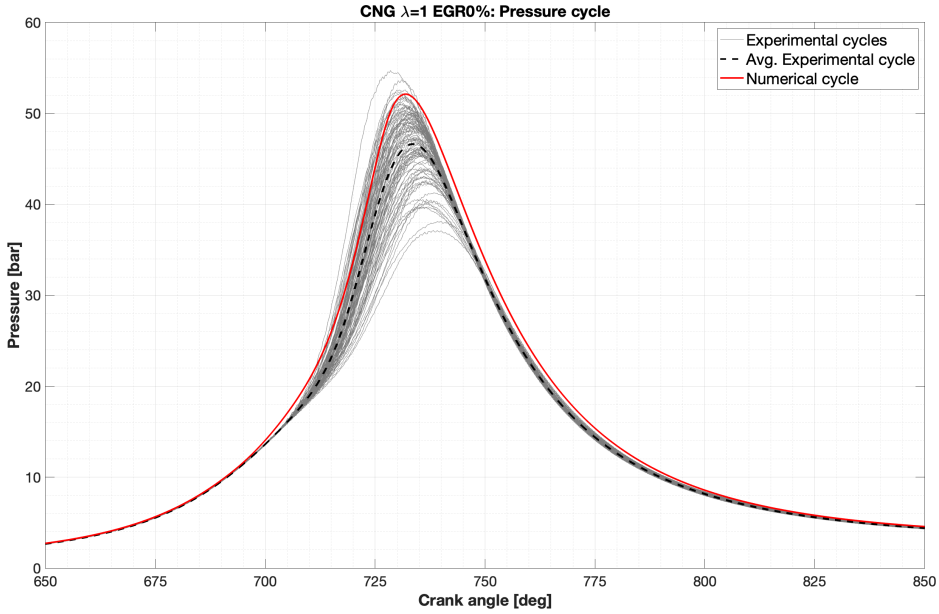

Figure 25: In-cylinder pressure time history of numerical and experimental cycles for CNG λ=1

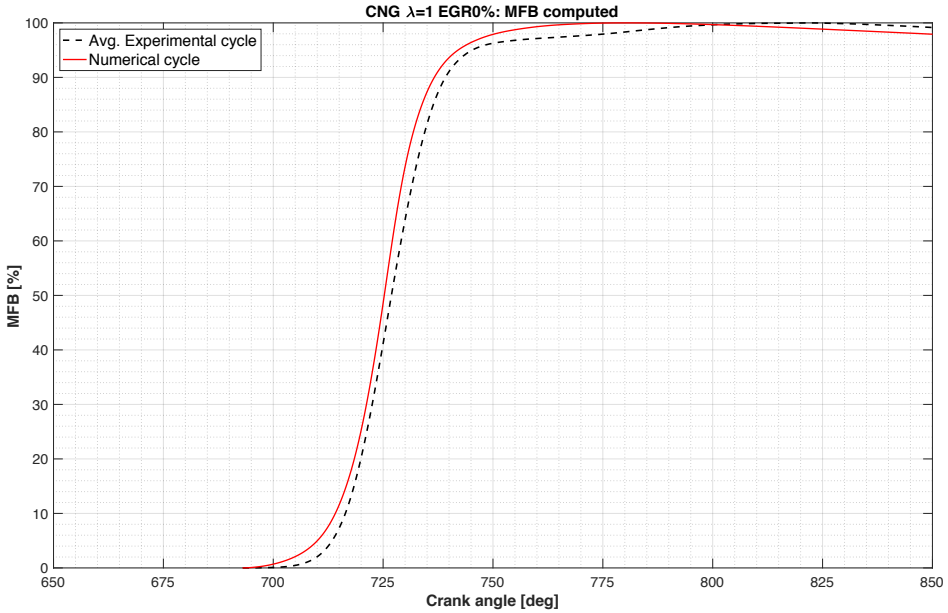

Figure 26: MFB computed of numerical and experimental cycles for CNG λ=1

In the case of pure methane, the simulation results seem to overestimate the in-cylinder pressure, that anyway is in the range between experimental minimum and maximum cycles. The overestimation of the peak pressure leads to a slightly anticipated heat release in the numerical result, with respect to the experimental data.

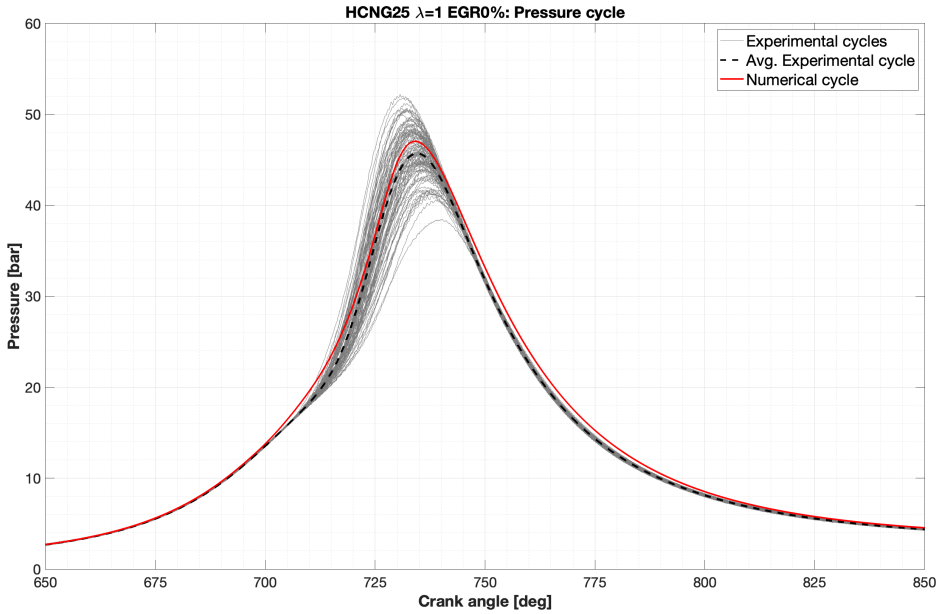

Figure 27: In-cylinder pressure time history of numerical and experimental cycles for HCNG25 λ=1

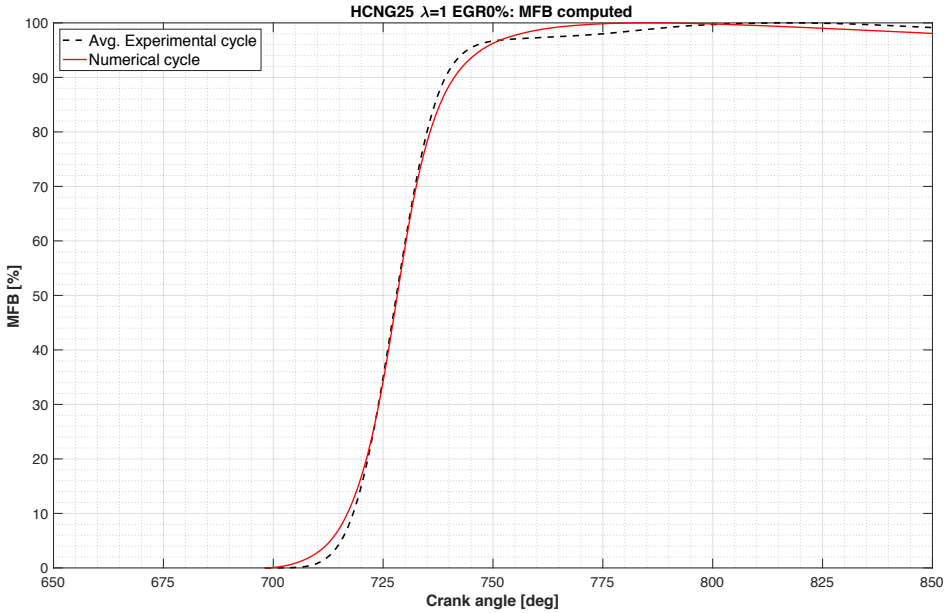

Figure 28: MFB computed of numerical and experimental cycles for HCNG25 λ=1

The figures 27 and 28 show that the model behaves perfectly also in the case of HCNG25. As final results of the validation process, in the case of stoichiometric condition, the main combustion and burning-rate parameters are compared between experimental and numerical (Figure 29):

- *PFP* : peak firing pressure;
- θ_{PFP}: crank angle relative to the peak firing pressure;
- *Δθ(90-10)*: combustion duration between 10% and 90% of burned mass fraction;
- *Δθ(90-10)*: combustion duration between 0% and 10% of burned mass fraction;
- *MFB50* : angle at which half of the mass has been burned.
- COV_{imep} : (coefficient of variation of *imep*), is an index of cycle to cycle variation.

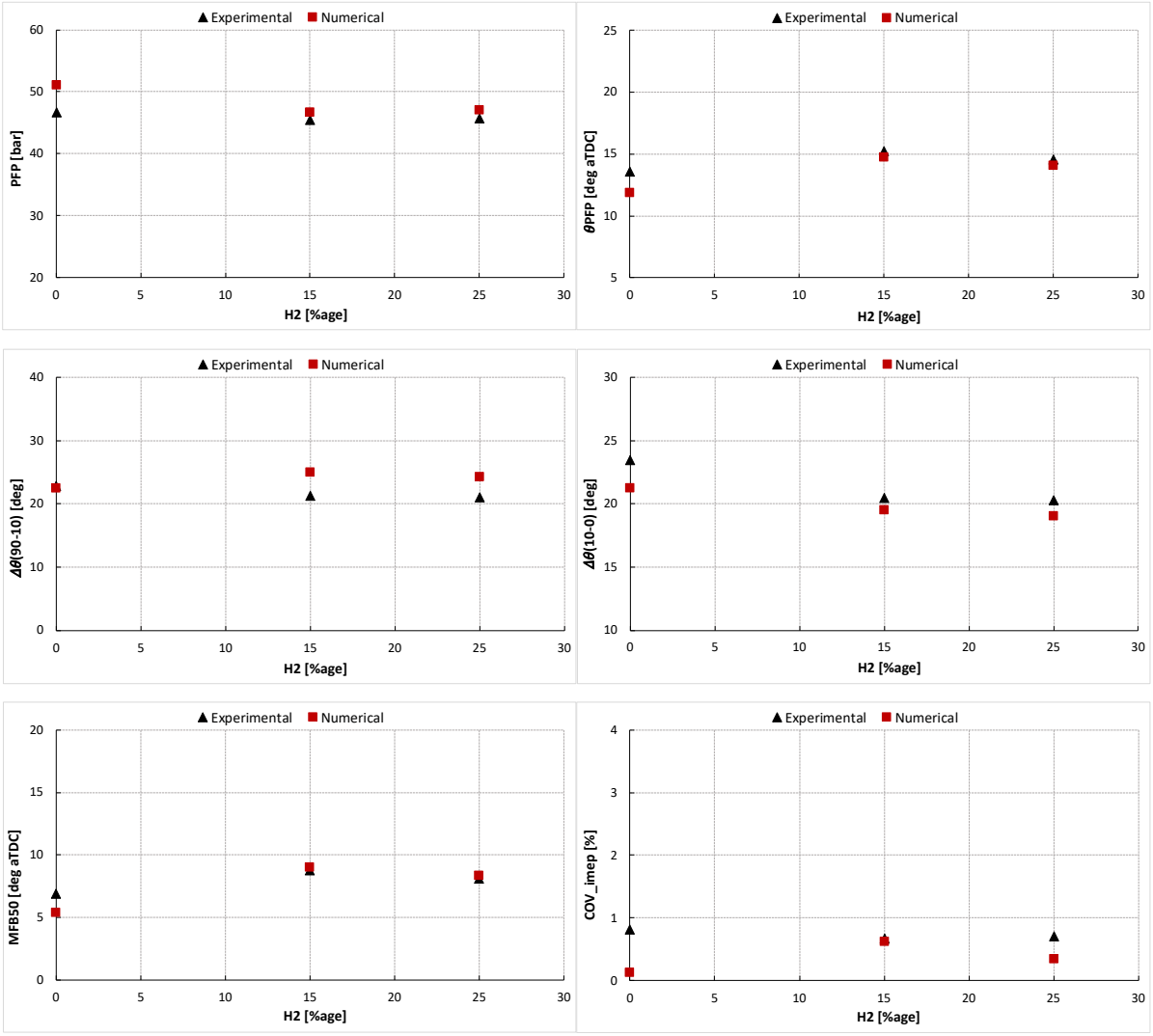

Figure 29: Results of the validation of the model for λ=1

The validation of the model for stoichiometric combustion is achieved, since the numerical results match the experimental one in every field with quite good accuracy. The model can predict the behavior of the engine running with three different fuel and can be used to predict also the dilution with exhaust gas (EGR).

2.3.3 Lean combustion λ=1.4

In lean combustion condition, the model could not be able to predict the behavior of the engine with the three different fuels, as in stoichiometric condition. In fact, following the same procedure it was not possible to validate the three cases with the same calibration parameters, just by changing the LFS table. In particular, it was necessary to use a set of calibration parameters for the two blends HCNG15 and HCNG25 and another set of parameters for CNG. For CNG the calibration parameters chosen are:

$$\begin{cases} C_{surf} = 13 \\ \alpha = 1.2 \end{cases}$$

In Figure 30 the comparison between the in-cylinder pressure time-history of the numerical and experimental cycles, in the case of CNG is represented, while in Figure 31 there is the comparison between the burned mass fraction (MFB) computed of the two datasets.

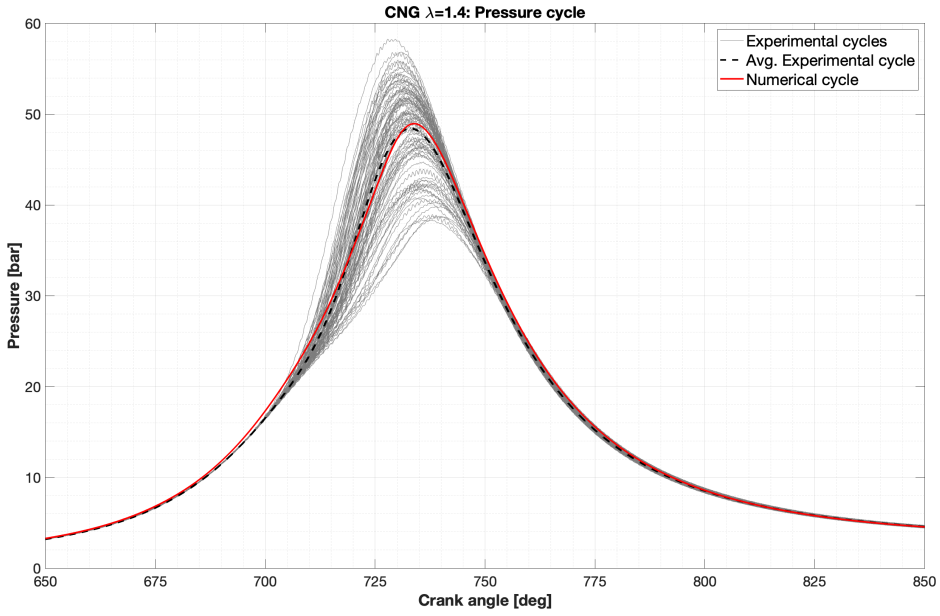

Figure 30: In-cylinder pressure time history of numerical and experimental cycles for CNG λ=1.4

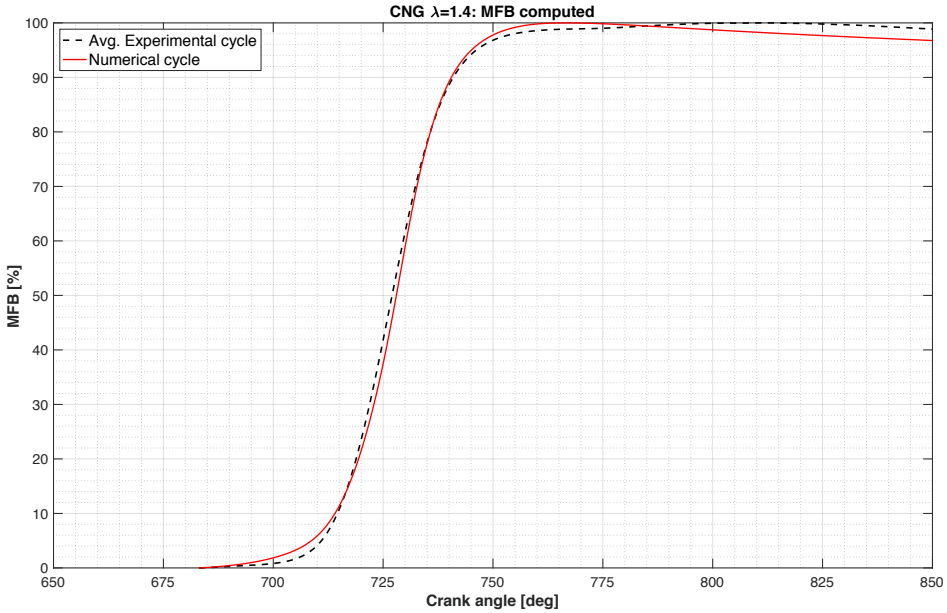

Figure 31: MFB computed of numerical and experimental cycles for CNG λ=1.4

In the case of NG-hydrogen blends, the calibration parameters used are the following:

$$\begin{cases} C_{surf} = 19 \\ \alpha = 1.9 \end{cases}$$

Figure 32 shows the comparison between the in-cylinder pressure time-history of the numerical and experimental cycles for HCNG15, while Figure 33 there is the comparison between the burned mass fraction (MFB) of the two datasets.

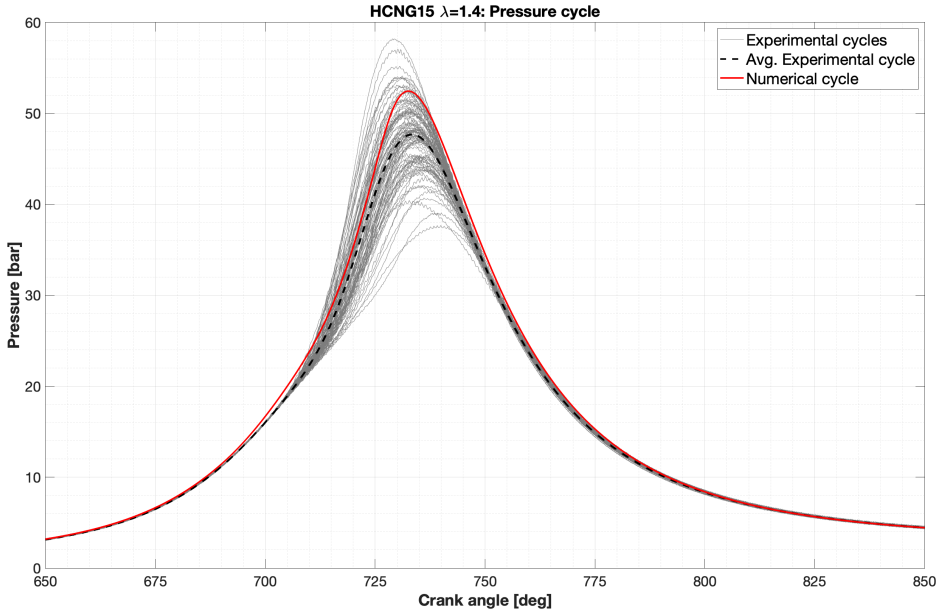

Figure 32: In-cylinder pressure time history of numerical and experimental cycles for HCNG15 λ=1.4

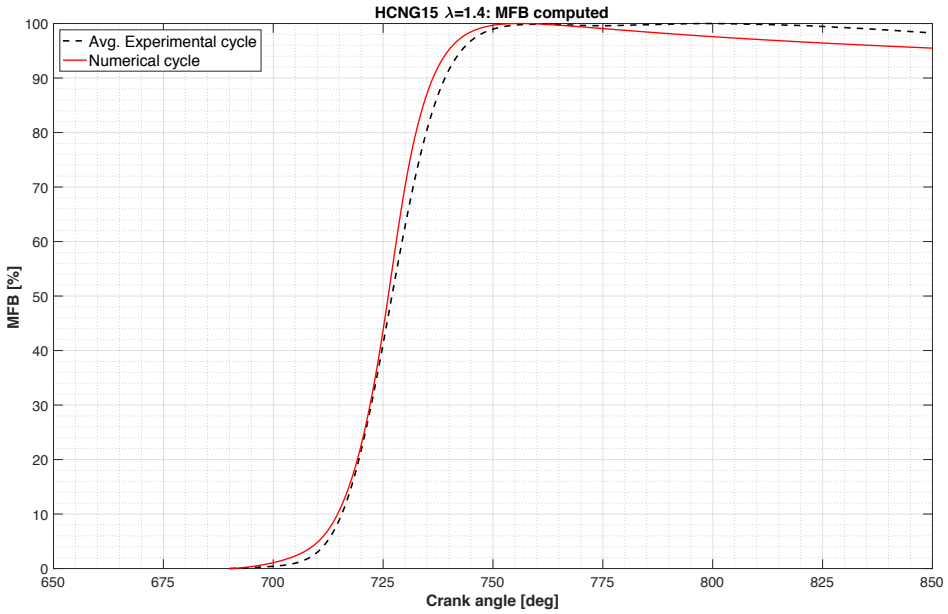

Figure 33: MFB computed of numerical and experimental cycles for HCNG15 λ=1.4

The pressure cycle inside the cylinder and MFB computed for HCNG25, compared with experimental data, are represented in figure 34 and 35. It is noticeable that in this case the heat release is retarded, because of a slightly underestimation in the pressure cycle.

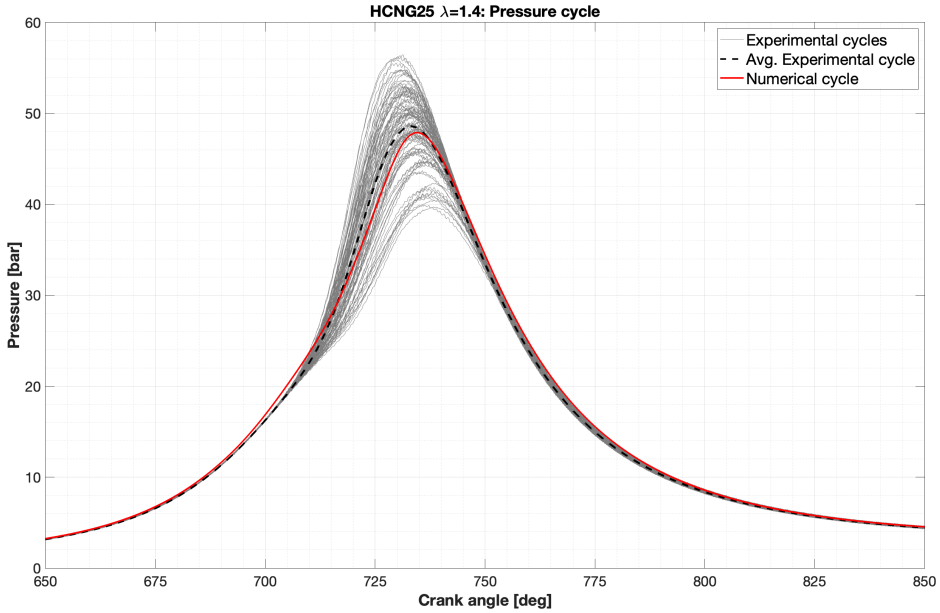

Figure 34: In-cylinder pressure time history of numerical and experimental cycles for HCNG25 λ=1.4

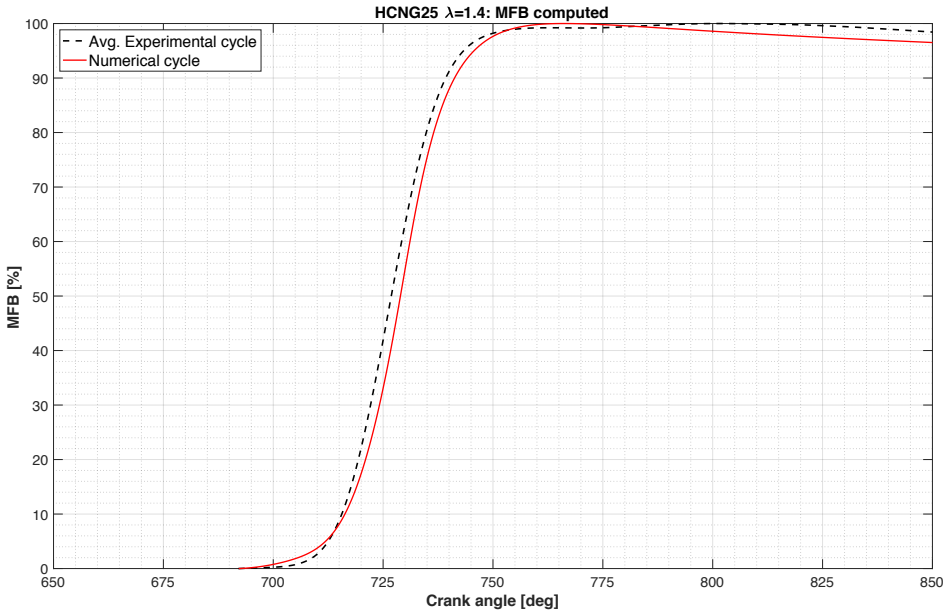

Figure 35: MFB computed of numerical and experimental cycles for HCNG25 λ=1

As final results of the validation process in the case of lean condition, the main combustion and burning-rate parameters, comparing experimental and numerical data, are shown in figure 36.

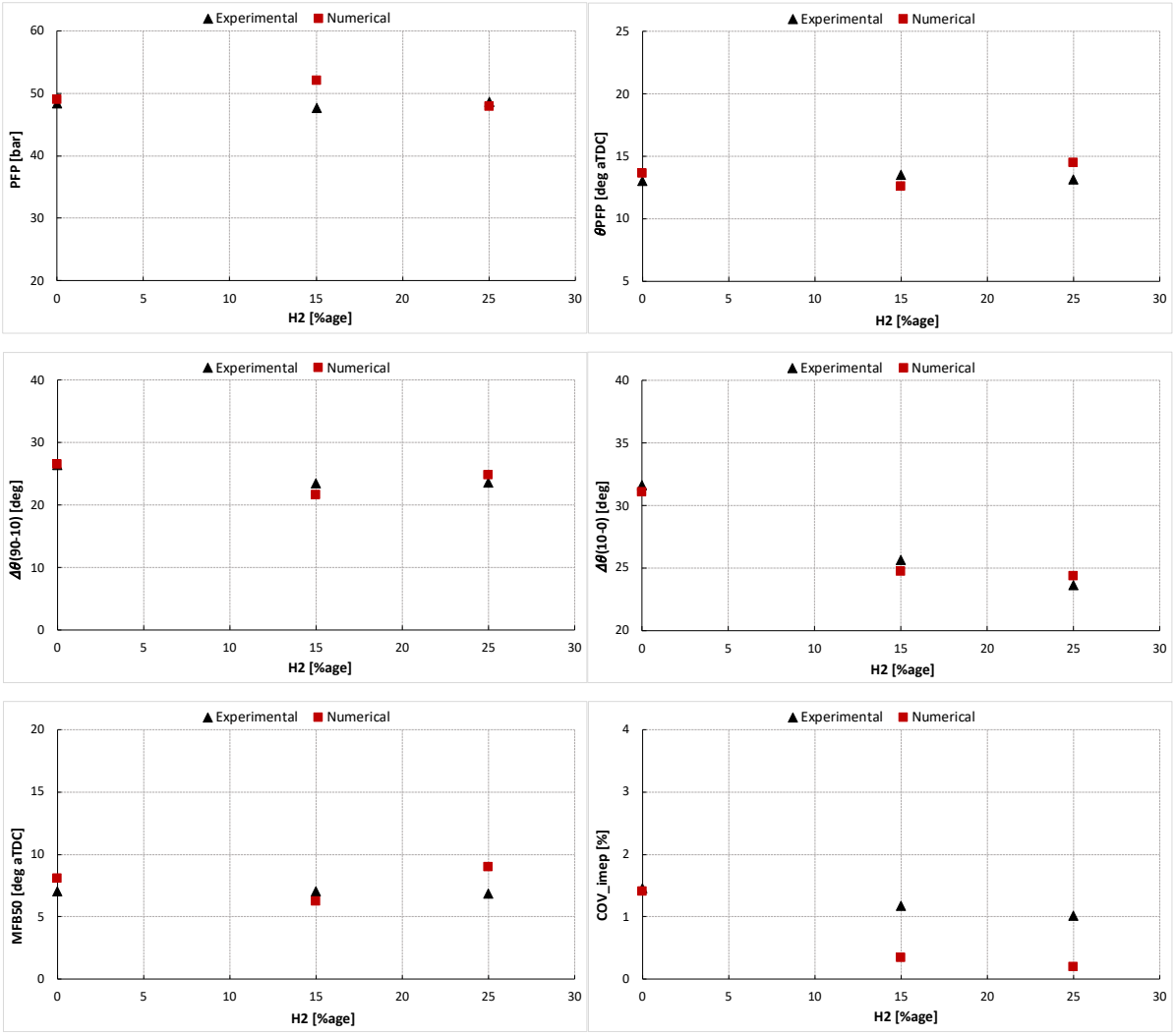

Figure 36: Results of the validation of the model for λ=1.4

Remembering that two different sets of calibration parameters has been used, one for pure methane and one set for the HCNG blends, also in the case of lean combustion, the model results to be validated, since the numerical results match the experimental data with good accuracy.

3. Results

3.1 EGR dilution

The technique consists of recirculating a portion of exhaust gas to the combustion chamber. actually, by supplying inert gas like carbon dioxide (CO_2) and water (H_2O), that because of their high thermal capacity, act as an absorbent and reduce the peak temperature during combustion. One of the most important advantage of EGR dilution is the significant reduction of the NO_x emissions; on the other side, the reduction of combustion temperature leads to reduction of indicated mean effective pressure (*imep*) and increase cycle to cycle variation (COV_{imep}) followed by a higher combustion duration and lower peak pressure. Increasing the EGR rate, at a given engine operating condition, the combustion instability increases, which results in the deterioration of engine performance. Therefore, the optimum EGR rate should be carefully determined in order to obtain the better trade-off between engine performance and emissions.

The purpose of this section is to study the combustion stability and engine performance of the three fuels previously investigated in the case of EGR dilution and in stoichiometric condition. To simulate the diluted combustion, some changes has to be made to the model. In particular, the intake pressure is raised almost linearly with the percentage of EGR, in order to keep the same fuel mass of the case without EGR. The chemical species of exhaust gas recirculated (CO_2, H_20) has to be taken into account. A very important parameter is the spark advance, that is increased to keep the same load as in non EGR case. Starting from a guess value, the spark advance is then corrected in order to keep the combustion phasing as close as possible to that of the non EGR case and the load fixed. The target decided for considering a simulation correct is $imep \approx 8$ bar and $MFB50 \pm 3deg$ with respect to the relative non EGR case. The procedure is summarized in the scheme below (figure 37).

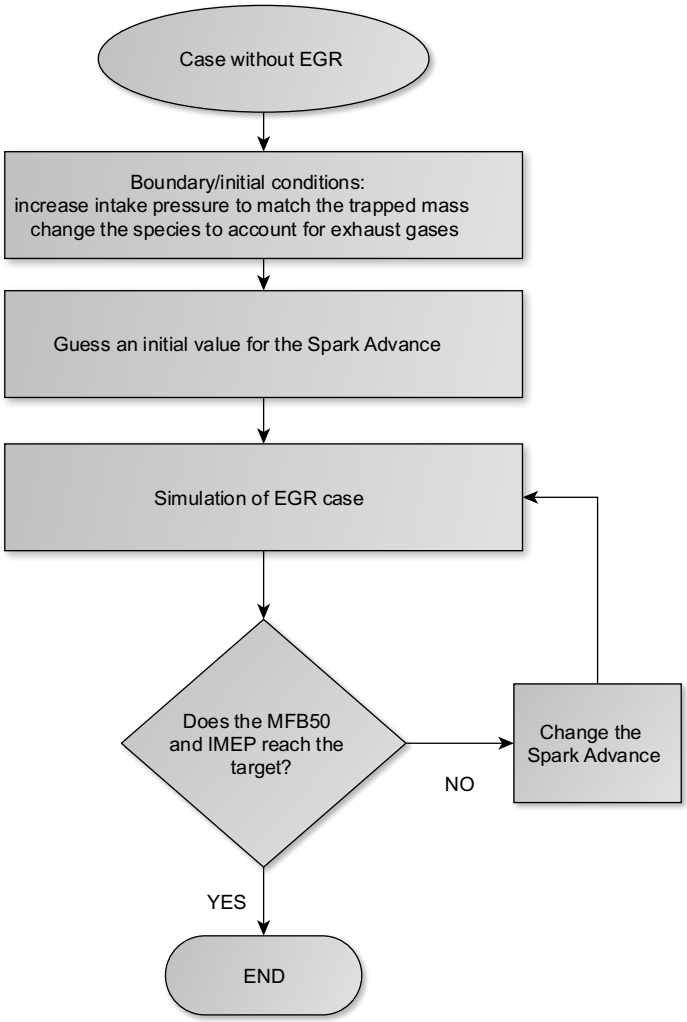

Figure 37: Scheme of the procedure for EGR simulation

In Figure 38 is represented the in-cylinder pressure in the case of CNG with the addition of different percentage of EGR, while figure 39 show the behavior of burned mass fraction, with particular attention to the MFB50 that should be in the target interval. In this case the simulation with 20% EGR, which is the limit for CNG, gives an incomplete combustion with MFB50 just outside the target range.

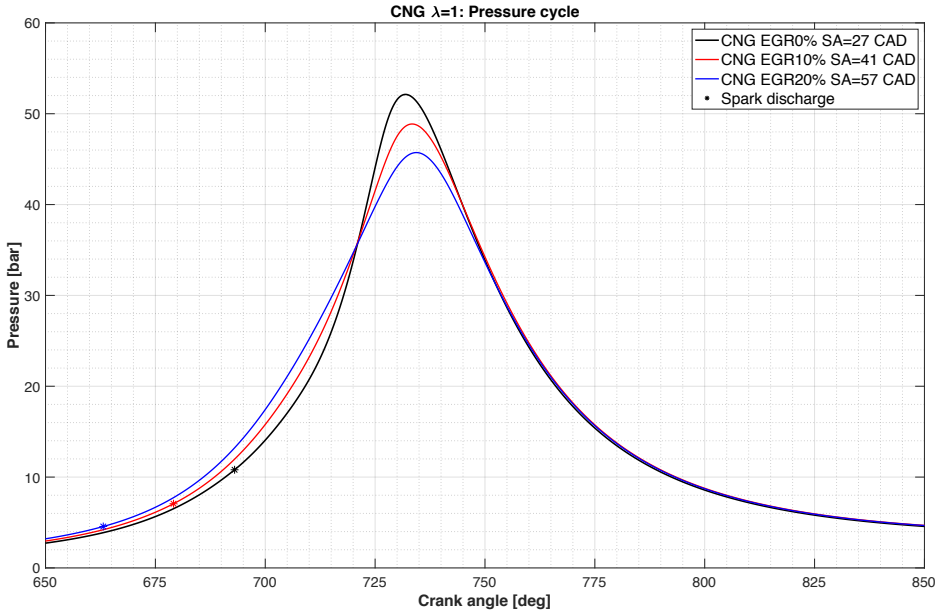

Figure 38: In-cylinder pressure time history of CNG λ=1, EGR cases

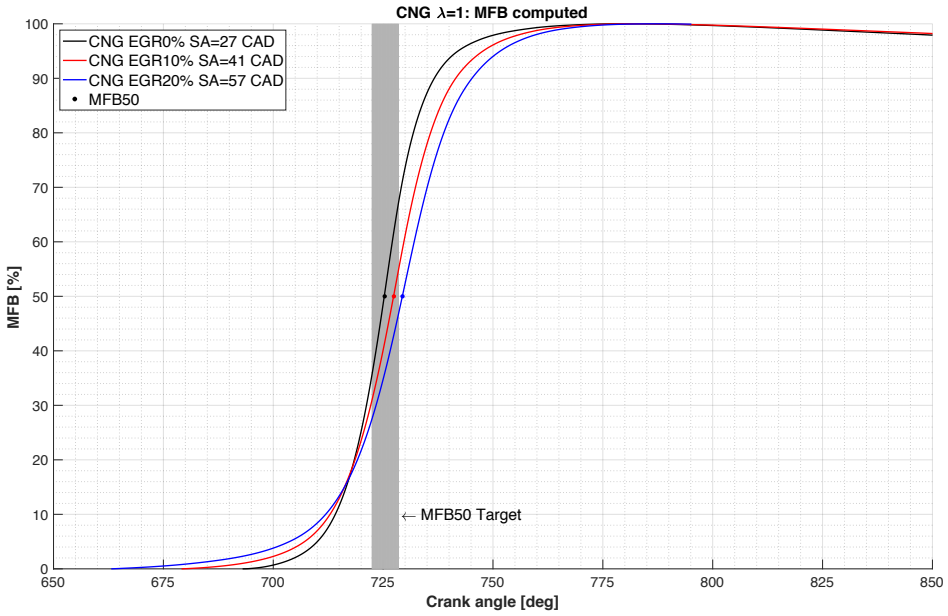

Figure 39: MFB computed for CNG λ=1, EGR cases

The same diagrams are shown for the two blends: HCNG15 pressure cycle in figure 40 and MFB in figure 41, HCNG25 pressure cycle in figure 42 and MFB in figure 43. It is noticeable that with hydrogen addition, the effect of EGR on combustion instability is less important. In

fact, low quantity of exhaust gas (10%) leads to better results than pure methane, in terms of combustion phasing with less spark advance increase. Moreover, the maximum quantity of EGR that can be tolerate is higher, as in the case of HCNG25 that is able to deal with 25% of EGR.

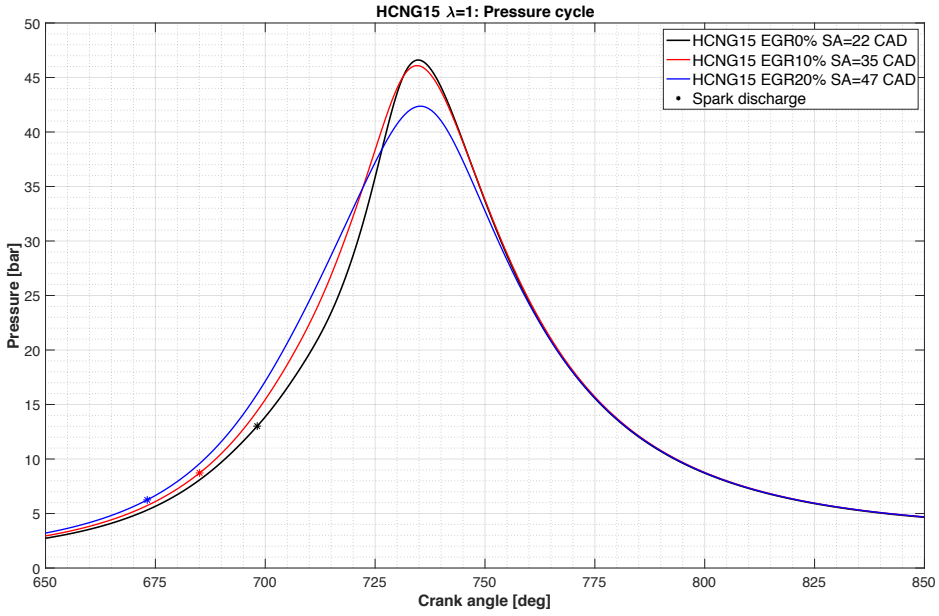

Figure 40: In-cylinder pressure time history of HCNG15 λ=1, EGR cases

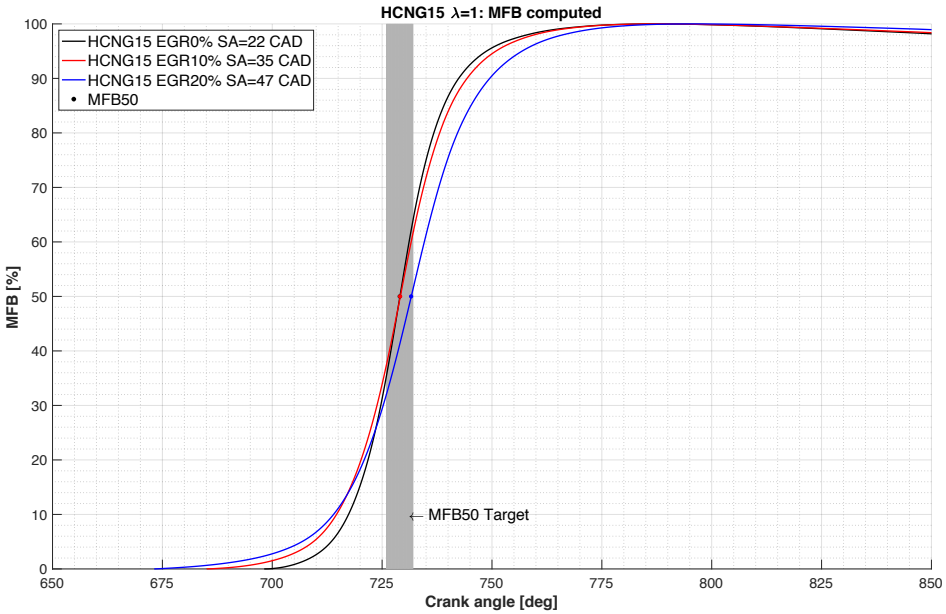

Figure 41: MFB computed for HCNG15 λ=1, EGR cases

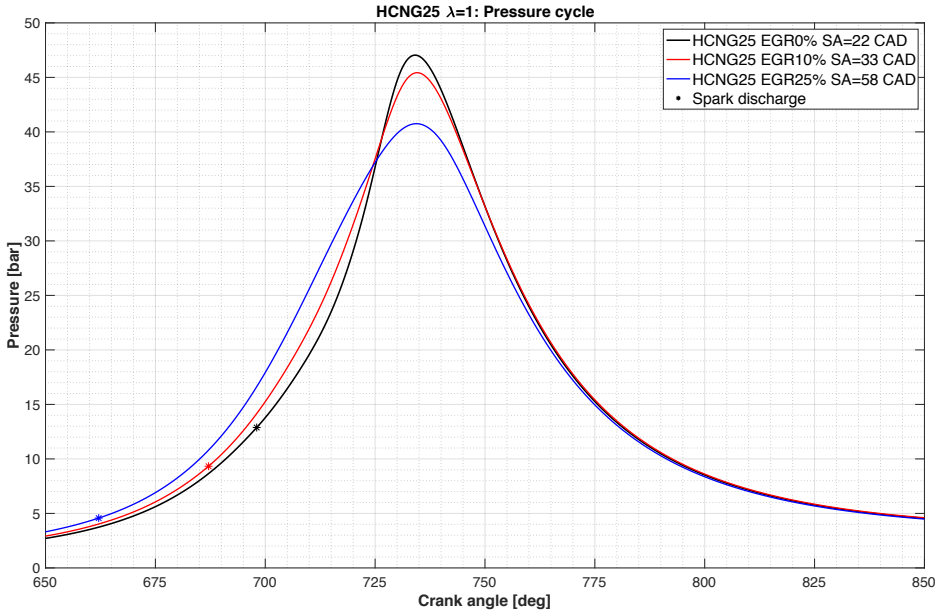

Figure 42: In-cylinder pressure time history of CNG λ=1, EGR cases

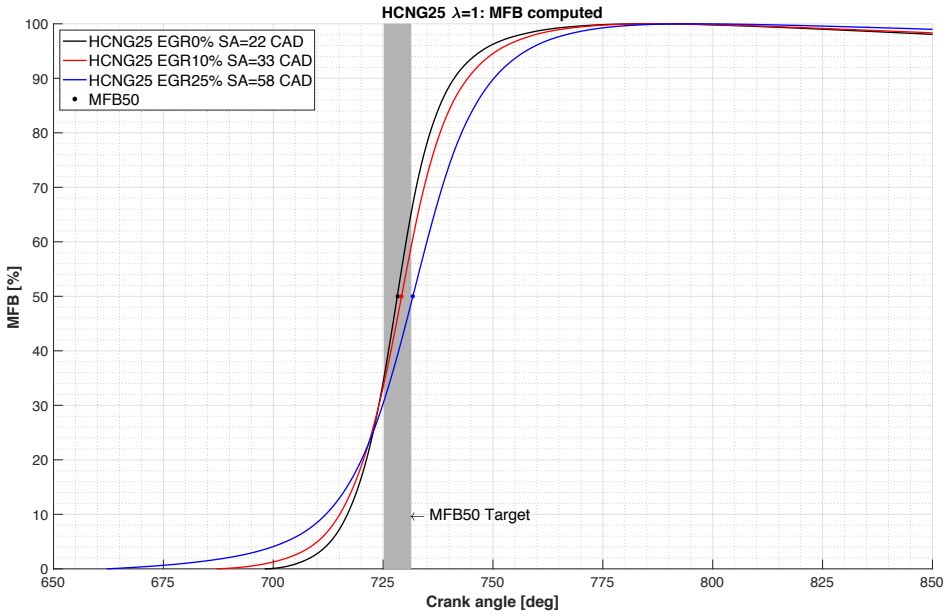

Figure 43: MFB computed for HCNG25 λ=1, EGR cases

The results show that in case of hydrogen addition, the combustion stability, in case of EGR dilution, is globally improved. The engine running with HCNG blends is able to work with higher EGR rate.

3.2 Effect of H2 and EGR on combustion

As final results of the simulations, the influence of hydrogen addition and EGR dilution on the combustion duration is analyzed. In fact, the addition of hydrogen is able to speed up the combustion, in particular in the early stages. This phase, addressed as the angular interval between 0% and 10% of burned mass fraction (MFB) is decreasing with the increase of hydrogen content, as represented in figure 44. In particular, adding 15% (in volume) of hydrogen, $\Delta\theta_{10\text{-}0}$ decrease by 8%, while adding 25% of hydrogen, $\Delta\theta_{10\text{-}0}$ decrease by 10%. EGR dilution, instead, has the opposite effect of increase the duration of first part of the combustion because of less concentration of reactants and lower temperature in the chamber. Comparing the effect of EGR dilution on the $\Delta\theta_{10\text{-}0}$ in the three different fuels, it is noticeable that the dilution influence more the pure CNG with respect to HCNG blends (figure 45 and table 6).

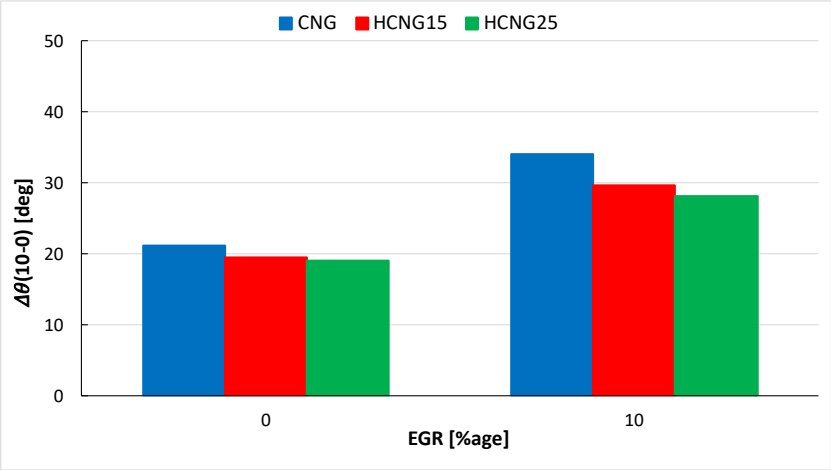

Figure 44: H_2 effect on combustion duration

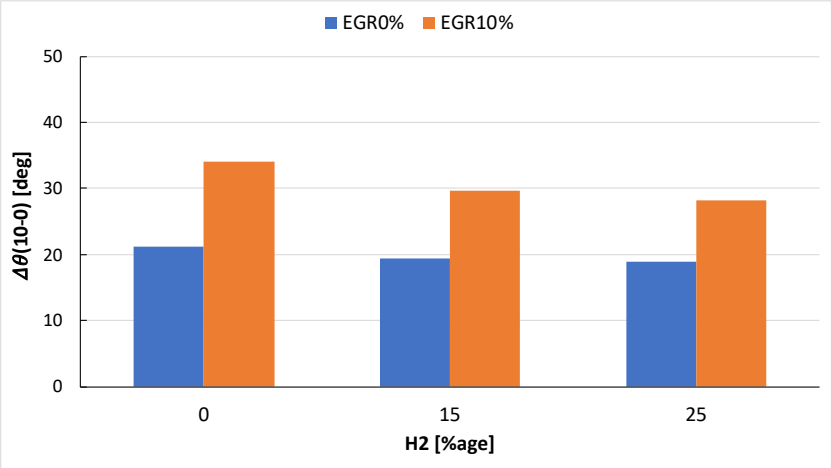

Figure 45: EGR effect on combustion duration

Increase in $\Delta\theta_{10\text{-}0}$ **in case of 10% EGR dilution**	
CNG	60%
HCNG15	52%
HCNG25	48%

Table 6: Percentage effect of EGR addition

The effect of hydrogen addition in the first stage of combustion process can be appreciated also in the following 3D images, that show the flame development inside the chamber. In figure 46 is represented the comparison between CNG and HCNG15 EGR0% in term of the fraction of methane, 10 degree after the spark advance. In figure 47 is represented the same comparison in term of temperature distribution inside the chamber. It can be noticed that the flame is more developed in case of hydrogen addition.

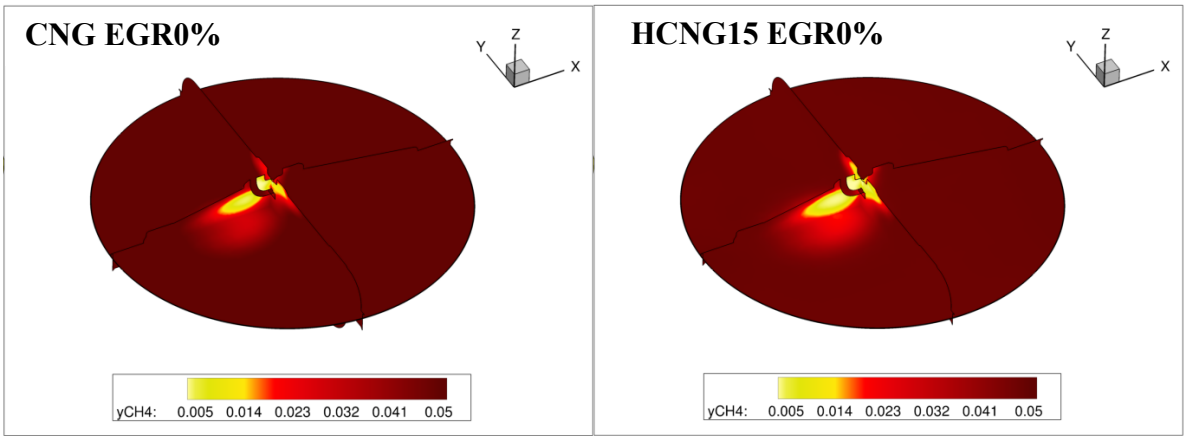

Figure 46: Fraction of methane at SA+10°, CNG vs HCNG15 EGR0%

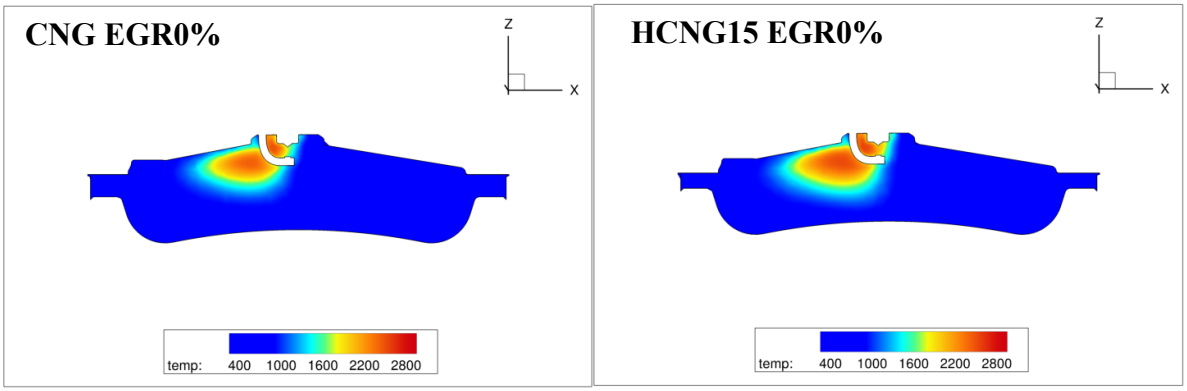

Figure 47: Temperature distribution at SA+10°, CNG vs HCNG15 EGR0%

In figure 48 is represented the comparison between CNG and HCNG15 EGR0% in term of the fraction of methane, 20 degree after the spark advance. In figure 49 is represented the same comparison in term of temperature distribution inside the chamber.

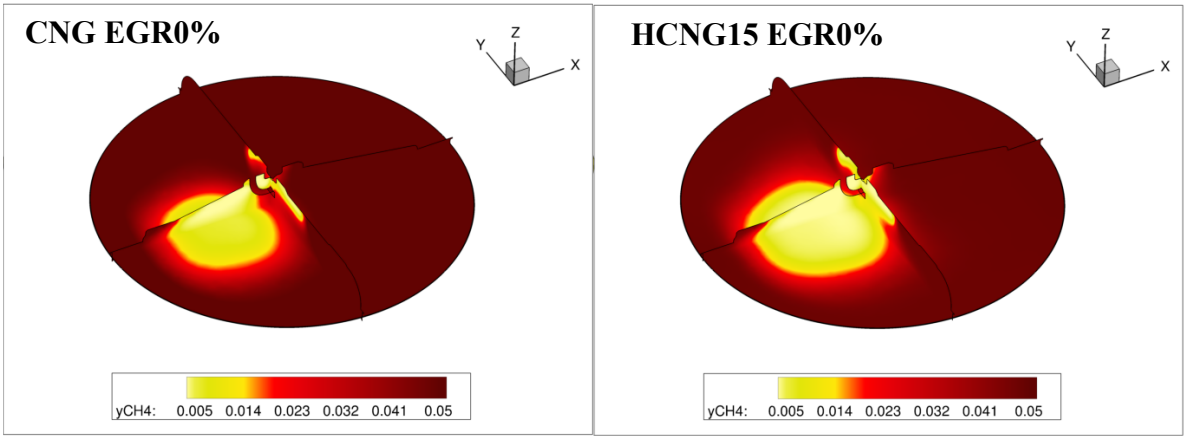

Figure 48: Fraction of methane at SA+20°, CNG vs HCNG15 EGR0%

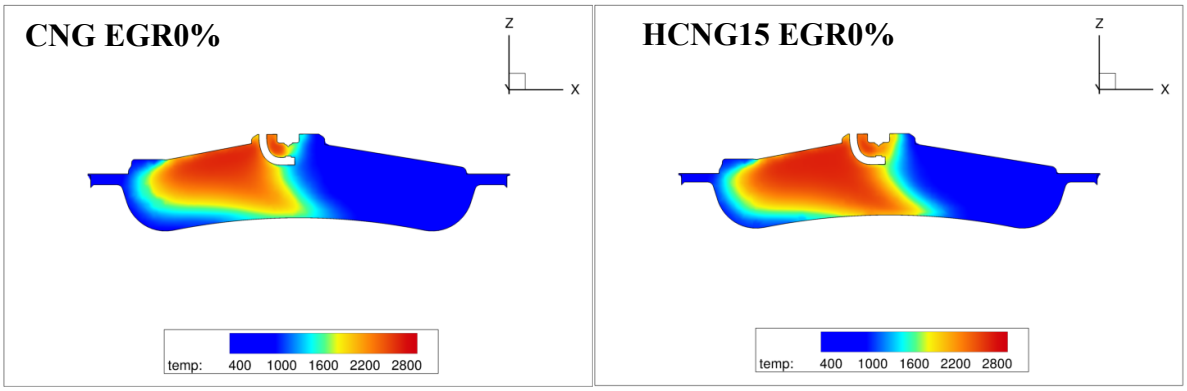

Figure 49: Temperature distribution at SA+20°, CNG vs HCNG15 EGR0%

The next comparison is between CNG and HCNG25 at 10% EGR. Figure 50 shows the methane fraction comparison, while figure 51 shows the temperature distribution comparison.

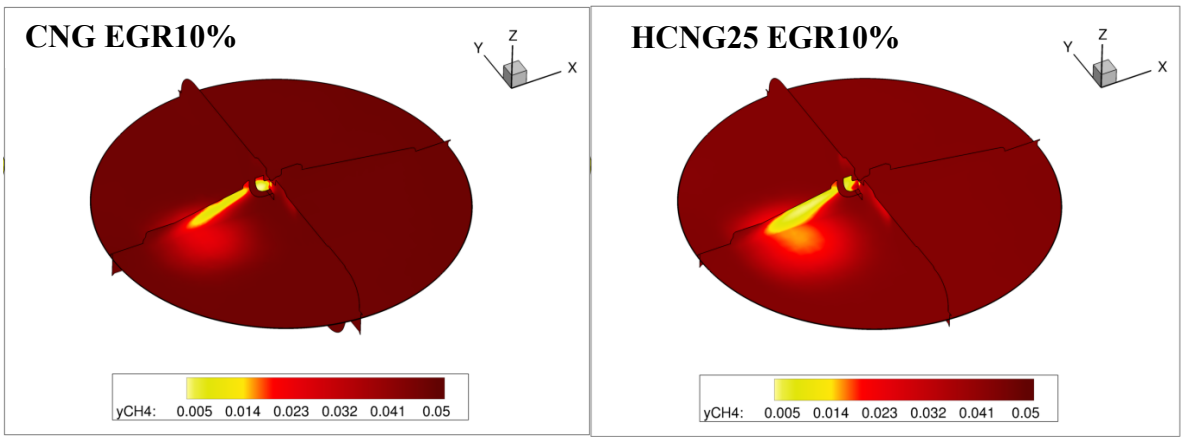

Figure 50: Fraction of methane at SA+20°, CNG vs HCNG25 EGR10%

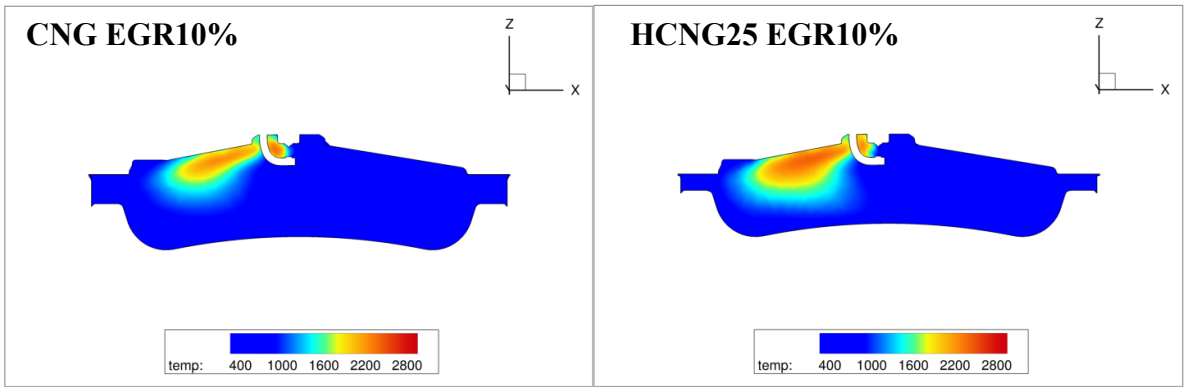

Figure 51: Temperature distribution at SA+20°, CNG vs HCNG25 EGR10%

In case of 20% EGR, as seen in the previous section, pure CNG is not able to complete the combustion. The addition of 15% of hydrogen can improve the combustion; in figure 52 is represented the comparison in terms of fraction of methane of the two cases, at top dead center (TDC). In figure 53, there is the temperature distribution.

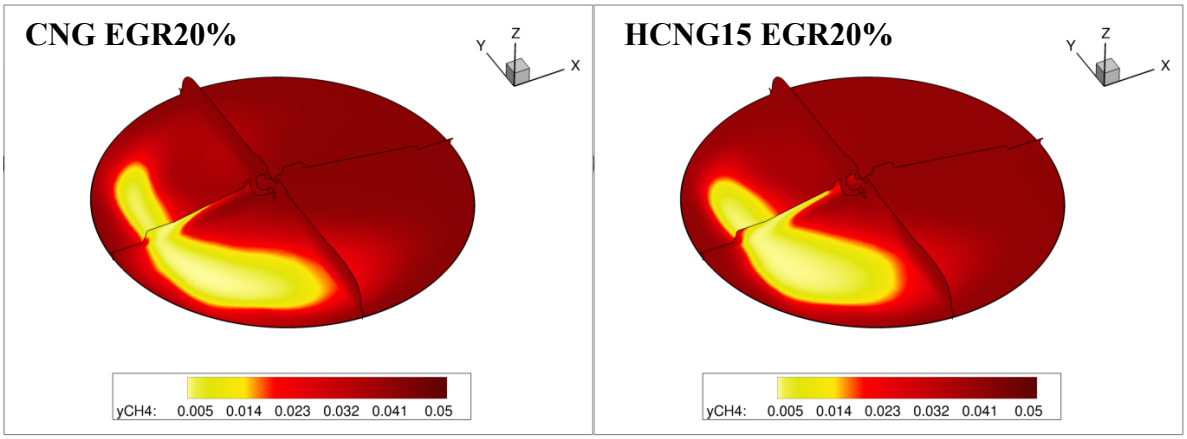

Figure 52: Fraction of methane at TDC, CNG vs HCNG15 EGR20%

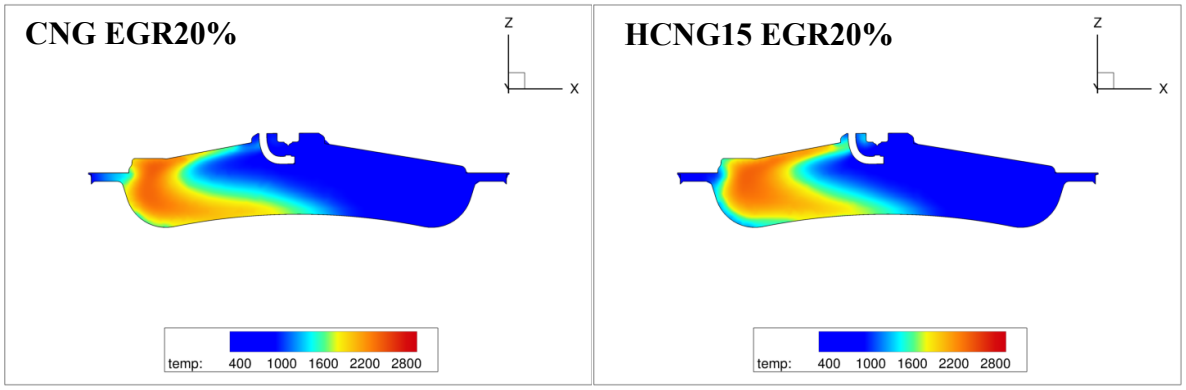

Figure 53: Temperature distribution at TDC, CNG vs HCNG15 EGR20%

In lean condition λ=1.4, the positive effect of hydrogen addition can be appreciate from figure 54, where it it shown the comparison between CNG and HCNG25 in term of the fraction of methane, at top dead center (TDC). In figure 55 is represented the same comparison in term of temperature distribution inside the chamber. Hydrogen increase the stability of combustion process and the development of the flame is more regular.

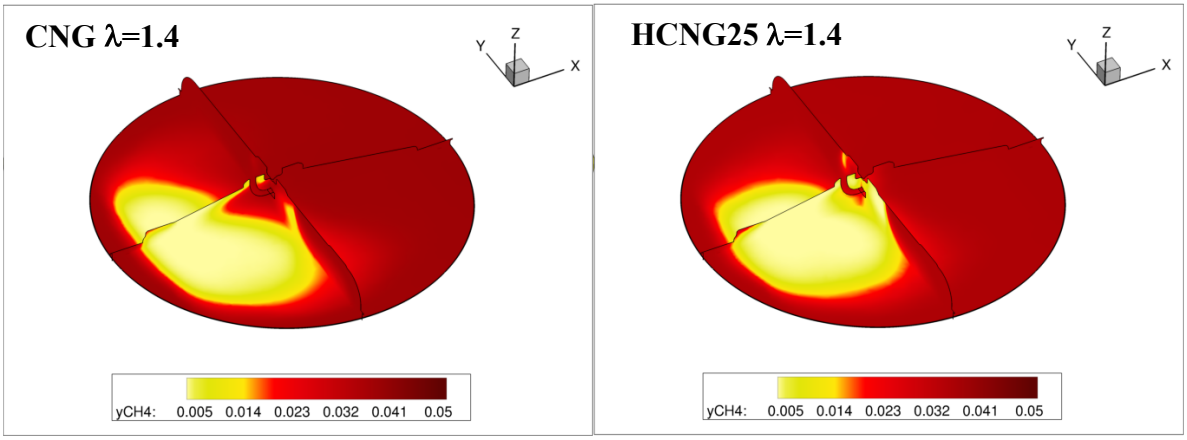

Figure 54: Fraction of methane at TDC, CNG vs HCNG25 λ=1.4

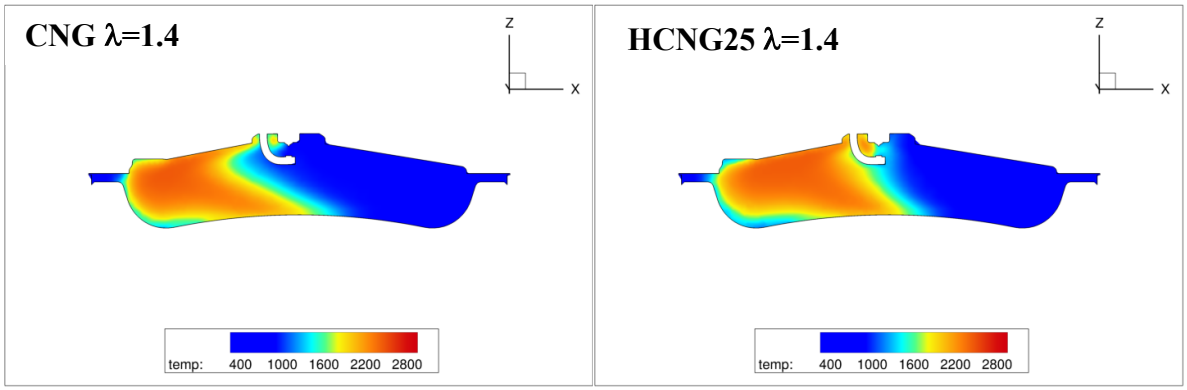

Figure 55: Temperature distribution at TDC, CNG vs HCNG25 λ=1.4

4. Spherical Flame model for Burning Velocities

4.1 Confined flame method

In this section, the analysis of flame propagation inside the combustion chamber is addressed, with particular attention to the turbulent burning velocity. Modern flame photographs define the position of the front or leading edge of the turbulent engine flame and prove that the 'shadow' of the inflamed zone, under normal engine conditions, is close to circle (only in presence of very high swirl a distortion of the flame shape occurs). Thus, the leading edge of the turbulent flame is, with good approximation, a portion of a surface of a sphere.

At practical laboratory conditions, however, the homogeneous air-fuel mixture is usually ignited inside a closed vessel and, hence, the heat released during flame propagation causes a pressure rise inside the vessel accompanied also by a temperature increase of the unburned mixture. Although it is well known that at early stages of flame propagation the pressure increases, it may be assumed to be negligible and hence the flame propagation is often assumed to be unconfined. Due to this fact, two methods for measuring S_{u0} from spherical flame propagation have been developed the literature, namely the confined flame (CF) and the unconfined flame (UCF) methods. The fundamental difference between those methods is that in the former, S_{u0} is extracted from the monitored pressure rise – $P(t)$ – inside the vessel, while in the latter method S_{u0} is extracted from the flame front radius trajectory – $R_f(t)$ – usually obtained by high-speed Schlieren photography.

In the confined flame model, the spherical flame with the radius of R_f is assumed to be ultimately thin and it separates the burned and unburned gas regions, as depicted in figure 56. Geometrical parameters such as the coordinates of the flame center and the radius of the flame circle can be identified. Initiated by a spark, the spherical flame propagates uniformly in all directions enabling fairly accurate determination of its total velocity by the flame radius only. The total spatial velocity of the flame can be simply computed as:

$$S_f = \frac{dR_f}{dt} \tag{35}$$

When considering a confined spherical flame method, some assumption has to be done [14]:

1. The spherical flame front is smooth and free from diffusion-thermal and hydrodynamic instabilities;
2. Both burned and unburned gas es are ideal;
3. The pressure is uniformly distributed inside the cylinder;
4. The unburned gas is compressed isentropically;
5. There is no dissociation or pre-flame reaction in the unburned gas;
6. Chemical equilibrium is reached immediately behind the flame front;
7. Radiation and buoyancy effects are negligible.

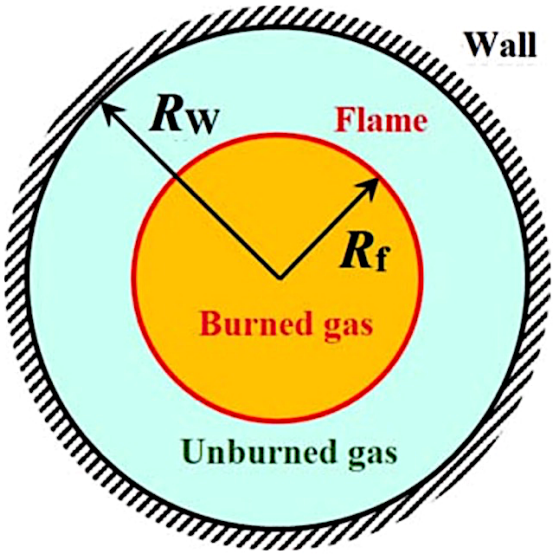

Figure 56: Spherical flame and burned/unburned zones

The confinement implies a pressure rise which is accompanied by temperature rise due to compression. Thus, the burned and unburned gas temperature, as well as its density, continuously increases during flame propagation. The confinement acts against the expanding burned gas and hence dR_f/dt is not equal to the burned gas velocity exiting the flame as it is assumed in the unconfined flame models. The actual flame front velocity – S_f – may be expressed as the sum of the expansion velocity of the burned gas inside the flame – S_g – that pushes the flame front forward, in addition to the turbulent burning velocity – S_u – at which the flame propagates into the unburned mixture [15]:

$$S_f = S_g + S_u \tag{36}$$

By knowing the burned mass fraction and the pressure evolution inside the chamber, it is possible to compute the flame radius and the turbulent burning velocity as follow:

$$R_f = R_w \cdot \left[\left(1 - \left(\frac{P_i}{P} \right)^{1/k_u} (1 - x) \right) \right]^{1/3} \tag{37}$$

$$S_u = \frac{dx}{dt} \frac{R_w^3}{3R_f^2} \left(\frac{P_i}{P} \right)^{1/k_u} \tag{38}$$

Combining the equations, the expansion speed of the gas can be expressed as:

$$S_g = \frac{R_w^3 - R_f^3}{3Pk_u R_f^2} \frac{dP}{dt} \tag{39}$$

4.2 Calculation of the flame speed

In the section the flame velocities are computed for Polito engine and compared with those of another engine, the GasOn engine. This second engine is characterized by higher compression ratio and higher turbulence intensity with respect to Polito. As case study another load point, 2000x6 bar is investigated, because it has been already simulated for both engines.

4.2.1 GasOn engine

The engine main specifications, for the single cylinder configuration, are shown in table 7 below.

Engine Specification

Bore	80.0 mm
Stroke	80.5 mm
Compression ratio	13.4
Displacement	405 cm^3
Valves per cylinder	4
Piston	Central shallow bowl
Ignition system	Mercedes coil (90 mJ) NGK spark plug (ILZKR8A)
Fuel system	Continental CNG DI-prototype
Intake valve	Opening duration: 169 CAD/ max lift: 8.5 mm
Exhaust valve	Opening duration: 200 CAD/ max lift: 8.5 mm

Table 7: Specifications of GasOn engine

The layout of the engine is represented in figure 57, while the numerical scheme for simulation setup is shown in table 8. The model was validated with the experimental data, which included in this case CNG test and relative EGR cases. The results of the validation are shown in figure 58.

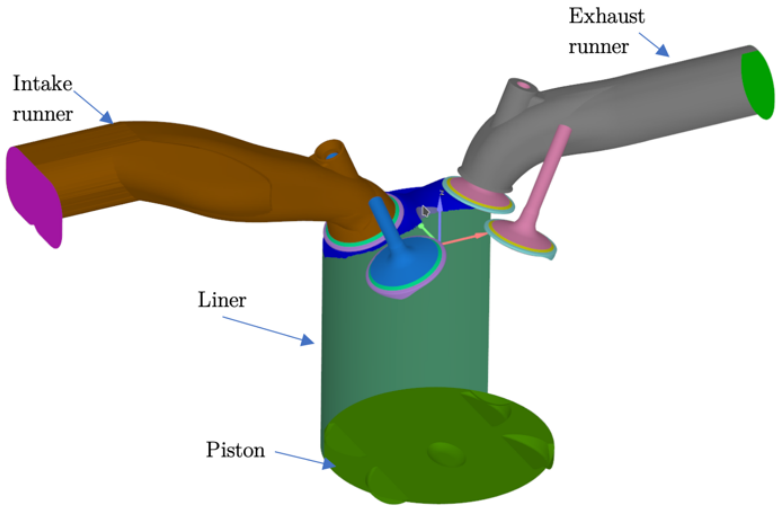

Figure 57:GasOn engine layout

Numerical Setup

Flow	Compressible
Gas simulation	Redlich-Kwong model
Numerical method	Implicit method
Turbulence model	RNG k-ε
Combustion model	ECFM
Ignition model	ISSIM
Heat transfer model	Angelberger

Table 8: Numerical Setup for GasOn engine

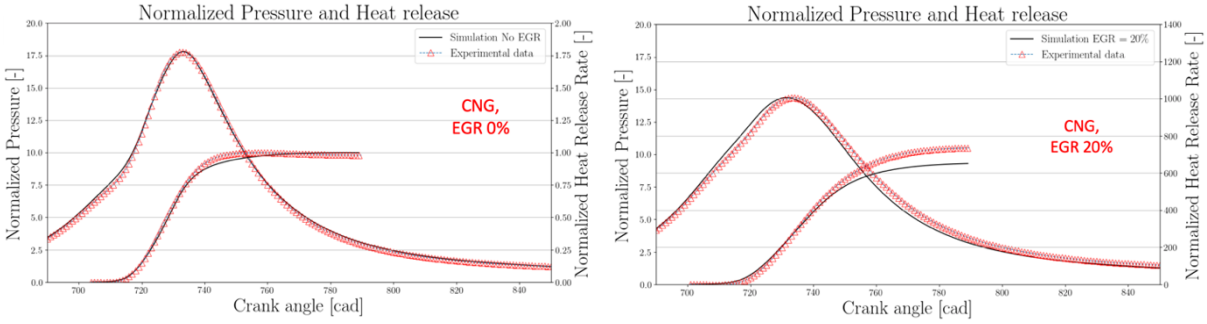

Figure 58: Validation of the model for GasOn engine

4.2.2 Results

The subdivision of the total flame speed into burning velocity and gas expansion speed is represented in figure 59 for Polito engine, while in figure 60 for GasOn engine.

In both engines, the global behavior of the flame speeds is the same in the various cases: the intersection points between mean gas speed and burning velocity is located near 722 CAD in Polito engine and near 720 in GasOn engine.

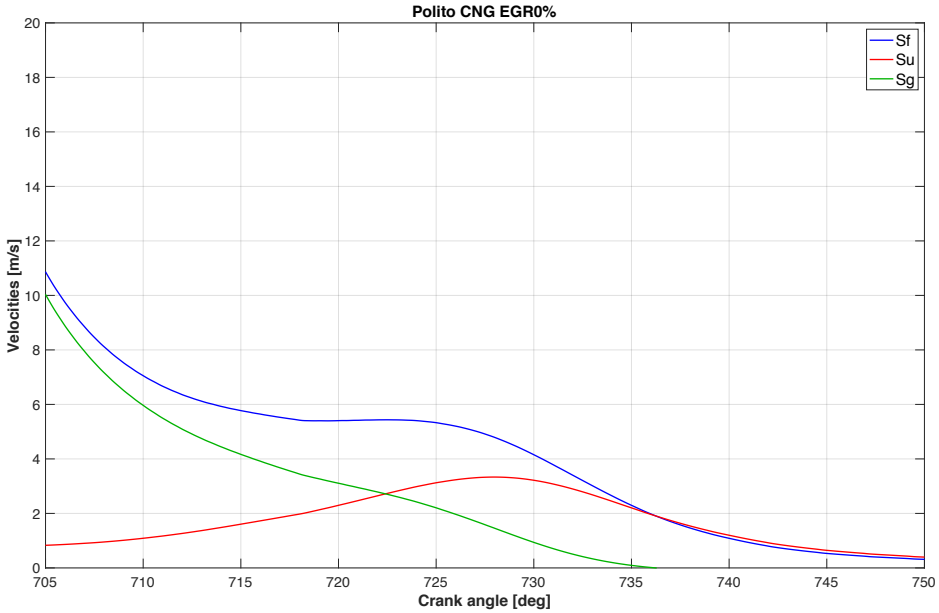

Figure 59: Flame speed calculated in Polito engine 2000x6 bar, CNG EGR0%

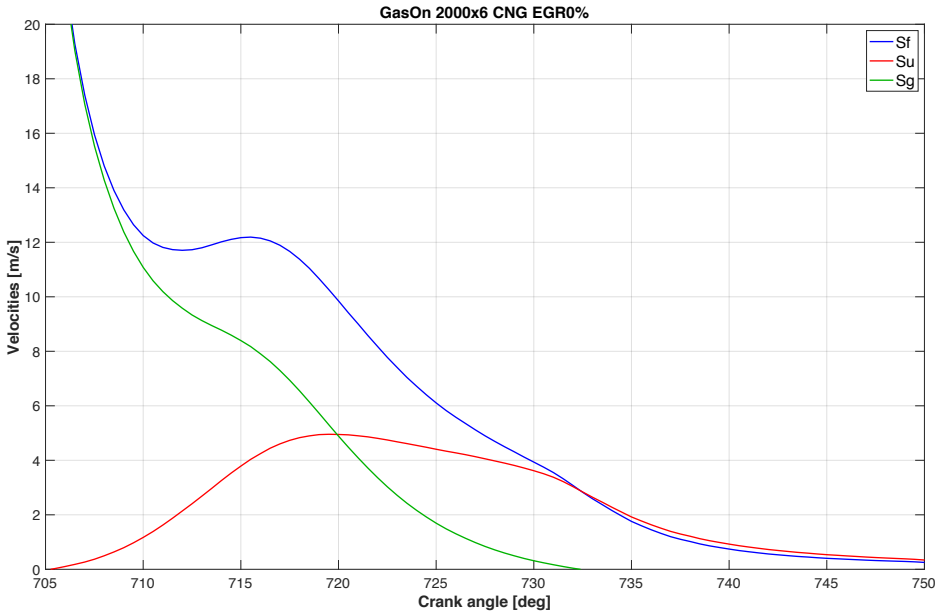

Figure 60: Flame speed calculated in GasOn engine 2000x6 bar, CNG EGR0%

It is important to underline an increase in the velocity with the addition of hydrogen, as expected in the theory, because of higher molecular diffusion property of hydrogen. This behavior is shown in figure 61 for Polito engine and in figure 62 for GasOn engine.

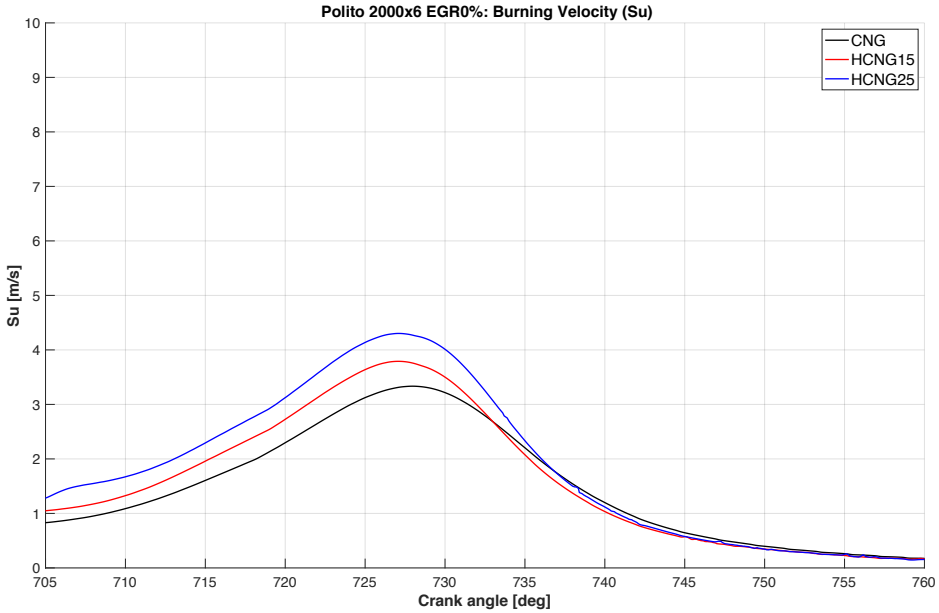

Figure 61: Effect of H_2 addition on burning velocity (Polito engine)

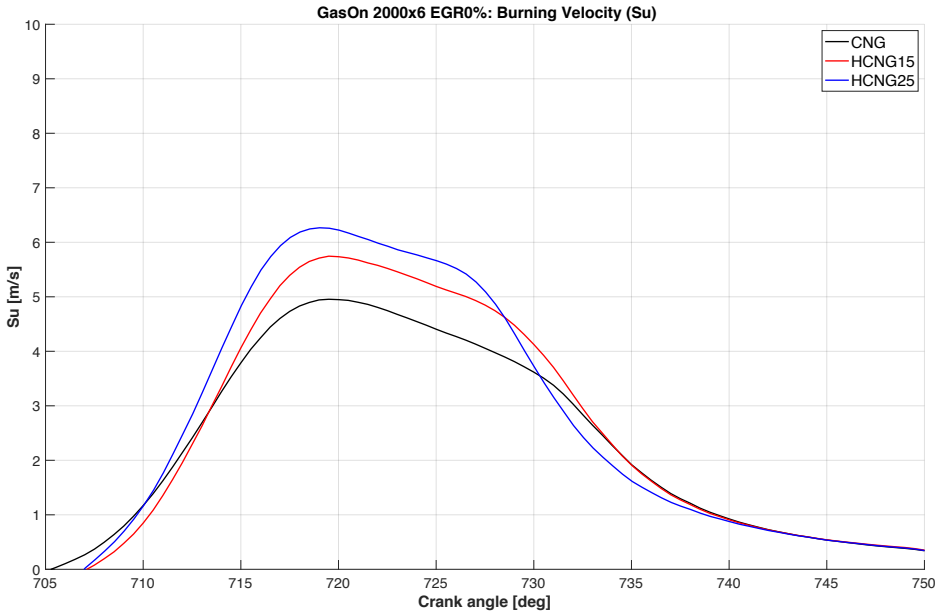

Figure 62: Effect of H_2 addition on burning velocity (GasOn engine)

The hydrogen addition leads to a quite regular increase in the burning velocity in both the engines.

The effect of EGR dilution is shown in figure 63 for Polito engine and in figure 64 for GasOn engine. Increasing EGR rate, in Polito engine the curve become flat and the combustion process

become unstable, while thanks to higher turbulence, GasOn engine can afford higher dilution level.

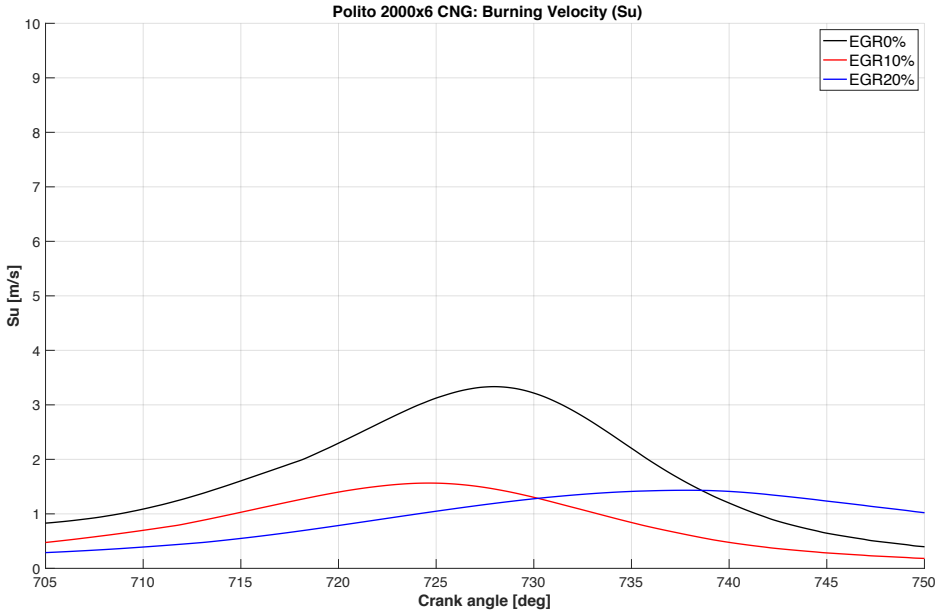

Figure 63: Effect of EGR addition on burning velocity (Polito engine)

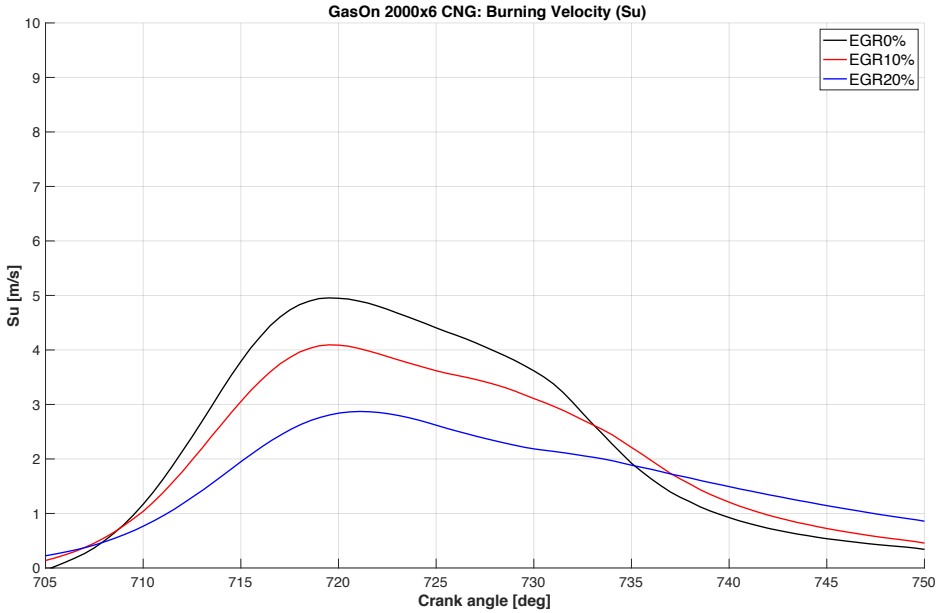

Figure 64: Effect of EGR addition on burning velocity (Polito engine)

The different behavior of the two engines in the flame propagation for the same fuel, is related to the different temperature and pressure conditions inside the chamber but mainly due to different turbulence inside the engines. From the comparison of burning velocities in figure 65 it is possible to appreciate how the turbulence influence the increase of burning rate, making the curve steeper in the first part.

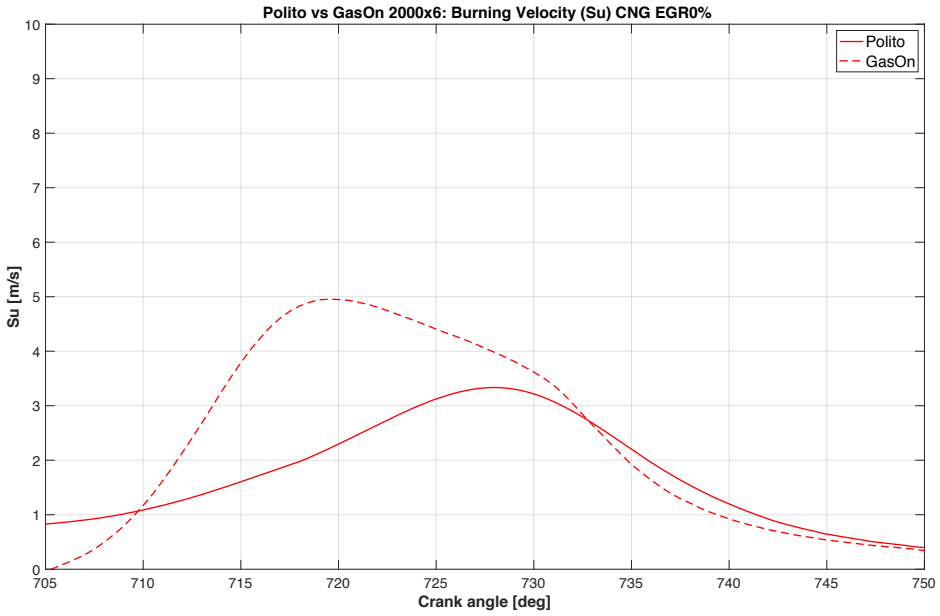

Figure 65: Burning velocity Polito vs GasOn engine

The ratio between the burning velocity of GasOn engine and Polito engine can be related to the ratio between the Damköhler number of the two engines and so to the major turbulence quantities, as in the following:

$$\frac{S_{u,GasOn}}{S_{u,Polito}} \propto \frac{\frac{1}{Da_{GasOn}}}{\frac{1}{Da_{Polito}}} \propto \frac{\left(\frac{u'}{L_t}\right)_{GasOn}}{\left(\frac{u'}{L_t}\right)_{Polito}} \tag{40}$$

The ratio *u'/Lt* will be called *turbulence ratio*. Figure 66 shows the comparison of burning velocity ratio and Damköhler number ratio of the two engines, while in figure 67 the burning velocity ratio and the turbulence ratio are compared. The present computations are in the case of CNG, but the same results are obtained also for HCNG blends.

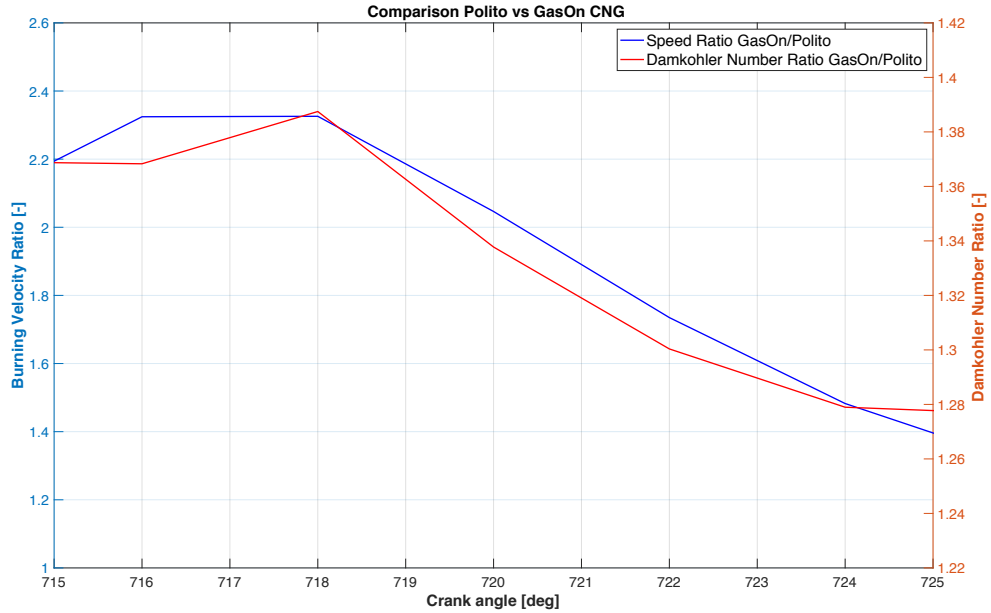

Figure 66: Comparison between velocity ratio and Damköhler number ratio

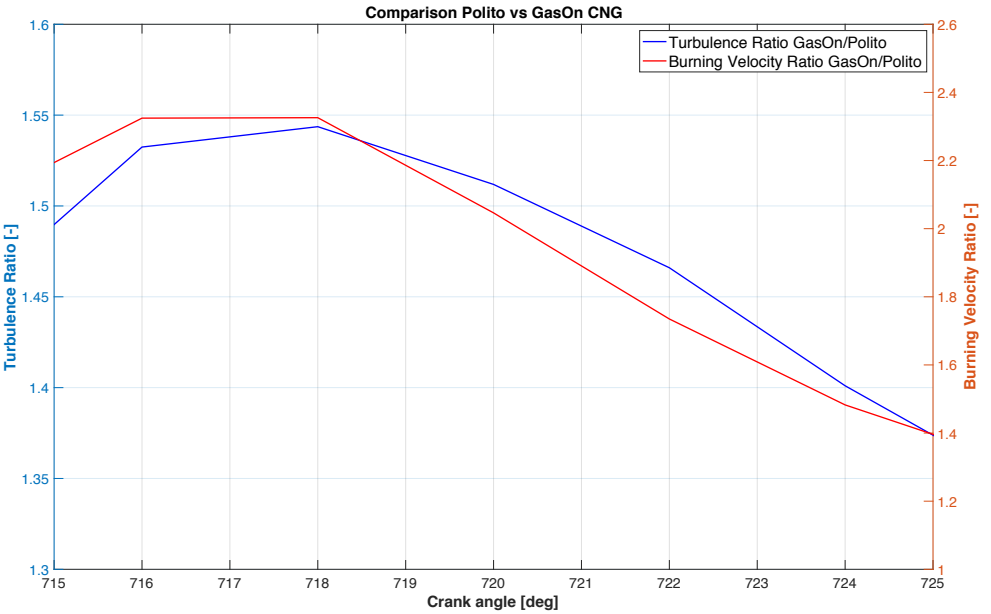

Figure 67: Comparison between velocity ratio and turbulence ratio

It can be noticed that the trend is the same for different ratios, in fact, the curve is first increasing until it reaches a maximum value before 720 CAD and then it decreases. The behavior of the two ratios underlines the fact that the difference in burning velocity of the two engines, is mainly due to the difference in the turbulence developed inside the engine.

Conclusions and future works

The objective of the thesis was to investigate the effect of hydrogen addition to methane in a NG engine addition through CFD simulations. The CFD model developed and implemented in CONVERGE software has been used also to predict the behavior of the engine in case of dilution of the in-cylinder charge with exhaust gas recirculated (ERG) in different percentage. The combined effects of hydrogen and EGR have been considered. The results of the simulations confirm the theory found literature, in particular the hydrogen addition to NG leads to a reduction in combustion duration. In particular, the first stage of heat release become faster, thanks to the burning properties and the higher diffusivity of hydrogen. The combustion stability is globally improved, hydrogen can be particularly useful in case of lean condition or diluted combustion and it can also increase the EGR tolerance of the engine. Diluted combustion can be an important way to reduce the temperature in the chamber and the emissions.

In the last part of the work, the burning velocity in the combustion process are computed following a spherical flame method. The results show that the burning speed is increased by hydrogen addition as expected, while lean condition and dilution lead to lower burning speed and thus to a less stable process. The burning velocity are compared with those calculate for a higher turbulence engine in order to assess the effect of turbulence. It leads to a faster flame propagation thanks to higher wrinkling and mixing and to an overall improved combustion.

As future works can be suggested to find a different method to deepen the study of the burning velocity in combustion process and to find a correlation that links the burning velocity to hydrogen percentage, EGR rate and turbulence characteristics of the engine.

References

[1] H. Chen, J. He and X. Zhong, “Engine combustion and emission fuelled with natural gas: A review,” *Journal of the Energy Institute,* vol. 92, pp. 1123-1136, 2019.

[2] M. Garg and R. Ravikrishna, “In-cylinder flow and combustion modeling of a CNG-fuelled stratified charge engine,” *Applied Thermal Engineering,* no. 149, pp. 425-438, 2019.

[3] M. Baratta, D. Misul, P. Goel and D. Laurenzano, “Experimental and Numerical Analysis of Diluted Combustion in a Direct Injection CNG Engine Featuring Post- Euro-VI Fuel Consumption Targets,” *SAE Technical Paper,* no. 01, p. 1142, 2018.

[4] M. Baratta and D. Misul, “Development of a method for the estimation of the behavior of a CNG engine over the NEDC cycle and its application to quantify for the effect of hydrogen addition to methane operations,” *Fuel,* no. 140, p. 237–249, 2015.

[5] M. Baratta, S. D'Ambrosio and D. A. Misul, “Performance and Emissions of a Turbocharged Spark Ignition Engine Fuelled with CNG and CNG/Hydrogen Blends,” *SAE Technical Paper,* no. 01, p. 0866, 2013.

[6] P. Kundu, I. Cohen and D. Dowling, Fluid Mechanics, 2012.

[7] J. H. Ferziger and M. Perić, Computational Methods for Fluid Dynmics, Springer, 2002.

[8] Convergent Science, *CONVERGE Manual v2.4,* 2017.

[9] S. B. Pope, Turbulent Flows, Cambridge, 2000.

[10] J. B. Heywood, Internal combustion engine fundamentals, McGraw-Hill, 1988.

[11] D. Veynante and L. Vervisch, "Turbulent combustion modeling," *Progress in Energy and Combustion Science,* no. 28, pp. 193-266, 2002.

[12] P. Goel, *3D-CFD Simulation of the Combustion Process in a NG Engine by Adopting a LFS Submodel from Detailed Kinetic Mechanism,* 2017.

[13] O. Colin, A. Benkenida and C. Angelberger, “3D Modeling of Mixing Ingition and Combustion Phenomena in Highly Stratified Gasoline Engines,” *Oil & Gas Science and Technology-IFP,* vol. 58, no. 1, pp. 47-62, 2003.

[14] O. Colin and A. Benkenida, “The 3-Zones Extended Coherent Flame Model (ECFM3Z) for Computing Premixed/Diffusion Combustion,” *Oil & GAs Science and Technology-IFP,* vol. 59, no. 6, pp. 593-609, 2004.

[15] M. Baratta, S. D'Ambrosio, D. Misul and E. Spessa, “Effects of H2 addition to CNG blends on cycle-to-cycle and cylinder-to-cylinder combustion variation in an SI engine,” in *2012 Spring Technical Conference of the ASME Internal Combustion Engine Division*, Torino, 2012.

[16] M. F. Brunt, H. Rai and A. L. Emtage, “The Calculation of Heat Release Energy from Engine Cylinder Pressure Data,” *SAE Technical Paper,* no. 981052, 1998.

[17] M. Faghih and Z. Chen, “The constant-volume propagating spherical flame method for laminar flame speed measurement,” *Sci. Bull.,* vol. 61, no. 16, pp. 1296-1310, 2016.

[18] A. Omari and L. Tartakovsky, “Measurament of the laminar burning velocity using the confined and unconfined spherical flame methods - A comparative analysis,” *Combustion and Flame,* no. 168, pp. 127-137, 2016.

Acknowledgements

Alla fine di questo lungo e incredibile percorso vorrei ringraziare innanzitutto i miei professori Daniela Misul e Mirko Baratta per avermi dato sempre fiducia e avermi dato la possibilità di lavorare in uno splendido team. Un ringraziamento di certo va a Prashant, per avermi guidato nel lavoro di tutti i giorni e per avermi dato consigli importanti.

Un grande pensiero e un bacione a tutta la famiglia, chi è qui presente, chi a casa e non è potuto venire, chi è lassù (…e difatti.. ci sono riuscito, so che sarai orgogliosa di me).

A mamma e papà, che mi avete sostenuto sempre nei momenti belli ma soprattutto in quelli brutti, se son arrivato fin qui lo devo anche soprattutto a voi. Grazie di cuore per avermi dato sempre un buon esempio a cui ispirarmi e una buona parola per spronarmi a migliorare sempre.

Isabella, senza di lei questo traguardo non sarebbe stato possibile. Grazie di essermi stata vicina sempre, di avermi aiutato senza riserve e di avermi motivato quando ne avevo più bisogno.

Ringrazio Amir e Mehrnoosh per come mi avete accolto a linkhouse e per questi tre anni passati a casa insieme.

Infine, un grazie a Fahed e Carlo. Insieme abbiamo condiviso buona parte del pesante percorso di studi, reso più leggero da tanta allegria e bei momenti che non saranno dimenticati (ora tocca a voi, wooooooork).